Acta Materialia 306 (2026) 121896

Contents lists available at ScienceDirect

Acta Materialia

journal homepage: www.elsevier.com/locate/actamat

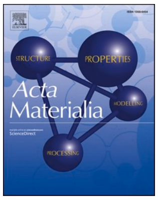

Refining hydrogen-dislocation interaction model for thermally activated plasticity in Fe-Cr-Ni austenitic steels: Analyzing stress-dependent activation volume

Yuhei Ogawa *, Akinobu Shibata

Research Center for Structural Materials, National Institute for Materials Science (NIMS), 1-2-1 Sengen, Tsukuba, 305-0047, Japan

ARTICLE INFO

Keywords:
Austenitic steels
Hydrogen
Dislocations
Thermally activated deformation

ABSTRACT

Understanding the role of diffusible solute hydrogen (H) as an obstacle to dislocation glide is essential for elucidating the solid solution-hardening mechanisms induced by H in Fe-Cr-Ni austenitic steels and other face-centered cubic (FCC) alloys. In the present study, we address this issue through an effective use of classical stress relaxation tests with a relatively long duration (~1000 s) at 295 K. A Type310S (Fe–24Cr–19Ni) austenitic stainless steel was examined after uniformly pre-charging ~8500 at ppm H under a pressurized high-temperature gaseous H_2 environment. The activation volume, V (*i.e.*, a material volume involved in an elementary obstacle-dislocation interaction), as a function of externally applied stress, was analyzed to probe the impact of H on thermally activated dislocation motion through a field of multiple obstacle types. A unified stress–V relationship was identified for both non- and H-charged specimens, in addition to an H-induced retardation of deformation kinetics under an equivalent stress level. These findings demonstrate that the primary obstacles to dislocation motion are alloying elements (and forest dislocations) even under the presence of H, with H contributing an additional activation barrier to overcome these inherent obstacle types.

1. Introduction

In the study field of hydrogen embrittlement in structural materials, there has been a long-standing debate over whether solute hydrogen (H) enhances or impedes dislocation motion in face-centered cubic (FCC) metals and alloys [1–9]. The authors have recently investigated the influence of H on the thermally activated deformation behavior of Fe-Cr-Ni austenitic stainless steels [10–12]. These studies have demonstrated that H consistently acts as a short-range obstacle to dislocation motion, marking a significant advancement in our knowledge on the fundamental role of H in material's plasticity. This paper advances our foregoing works by examining the specific nature of H–dislocation interactions and their influence on the kinetics of plastic flow. Particular emphasis is placed on how H modifies the activation parameters for dislocation glide in the presence of other intrinsic obstacles inherent to the material.

It is well established that interstitial alloying of carbon (C), nitrogen (N), and H causes considerable solid solution-hardening—manifested as increased yield and flow stresses—in Fe-Cr-Ni austenitic stainless steels [13–18]. The rationales behind solid solution-hardening by C and N have extensively been studied, with proposed explanations including lattice expansion due to their occupation of octahedral interstitial sites in FCC lattice [13,14,17,19], as well as the formation of atomic complexes between C/N and substitutional atoms [15,16,20]. In contrast, the fundamental understanding of solid solution-hardening by H—its atomic size being the smallest among all elements [21]—remains incomplete, particularly given that its hardening effect is often comparable to that of C and N [5,22,23]. A major challenge in elucidating the atomistic mechanisms responsible for H-induced solid solution-hardening lies in the high diffusivity of H atoms in austenite even at ambient temperatures (10^{-16}–10^{-15} m^2/s [23]), as estimated by extrapolating the diffusion data acquired at > 400 K [24–26]. This large mobility makes the detection of their interactions with moving dislocations challenging, despite remarkable advances of analytical techniques for H in metals over the latest few decades [27,28].

The solid solution-hardening by interstitial atoms in austenitic steels possibly increases both the effective and internal stress components [15,18,29]. Based on the classical dislocation theory, the former arises from the resistance to dislocation motion by short-range (on the order of few interatomic distances) obstacles, the overcoming process of which can

---

* Corresponding author.
E-mail address: OGAWA.Yuhei@nims.go.jp (Y. Ogawa).

https://doi.org/10.1016/j.actamat.2026.121896
Received 13 July 2025; Received in revised form 3 December 2025; Accepted 2 January 2026

be aided by coherent thermal vibration of metallic atoms (*i.e.*, thermally activated dislocation motion). Contrarily, the latter component originates from relatively long-range barriers that require larger activation energies to be overcome. This distinction in obstacle property renders effective stress sensitive to temperature, time, and strain rate, whereas internal stress remains largely unaffected by these variables [30–32]. Toward the roles of solid solution elements in affecting the deformation kinetics *via* these stress components, a classical yet robust method is the so-called thermal activation analysis based on transient mechanical tests [30,33–40]. Specifically, two key parameters—activation volume and strain rate sensitivity—offer valuable and statistically significant insight into obstacle-dislocation interactions [30,33,36,37,39,40]. Activation volume probes the material volume involved in each elementary thermal activation event (*i.e.*, obstacle extent and density), whereas strain rate sensitivity, inversely proportional to activation volume, quantifies the obstacle's sensitivity to thermally activated overcome [30,41,42]. These techniques have been effectively employed to study plastic deformation kinetics under the presence of both non-diffusible [33,35,36,39] and diffusible [43–45] solute species.

Regarding the diffusible H in austenitic stainless steels, room temperature stress relaxation and creep tests were systematically performed by the present authors for an AISI Type310S (Fe-24Cr-19Ni) uniformly charged with ~9000 at ppm H [10,12]. Standard tensile tests were performed and interrupted at predetermined strain levels, followed by displacement-holding or load-holding. Thanks to the elevated flow stress level associated with solid solution-hardening at the start of mechanical transient, H-charged specimens exhibited significantly larger relaxation stress-drop and creep strain, in agreement with previous findings by other researchers [6,46,47]. Importantly, these alterations in deformation behavior were consistently accompanied by a reduction in activation volume and an increase in strain rate sensitivity. Such changes in activation parameters substantiate that *H atoms act as short-range obstacles with more localized and thermally activatable characteristics compared to other obstacles* (*i.e.*, primarily alloying elements and/or forest dislocations for FCC solid solution alloys) inherent to the material. This behavior underscores the role of H in enhancing effective stress, thereby causing solid solution-hardening [5,23]. In essence, under the flow stress level of H-charged specimen—comprising both the material's intrinsic flow stress and the additional effective stress induced by H—*H atoms themselves might be promoted into primary rate-controlling obstacles as alternative to alloying elements or forest dislocations* [10]. Owing to the elevated flow stress, under which those two inherent obstacle types are readily surmountable, the kinetics of plastic deformation may be governed predominantly by the process of dislocations to overcome H, giving rise to a superficially greater magnitude of thermally activated deformation.

The interpretation described above is physically sound from a macroscopic perspective. Nevertheless, in a microscopic sense, a holistic picture on the functions of solute H, as a rate-controlling obstacle, is still elusive and indistinct. In previous studies employing thermal activation analysis, efforts have been mainly directed toward refining the measurement methodology of activation parameters [30,41,48–51], while little attention has been given to the mechanical conditions under which those parameters were evaluated. Even in the authors' prior works [10,11], comparisons were limited to fixed values of activation volume in non- and H-charged specimens, each assessed under their respective flow stress levels. Such comparisons provide only partial and fragmented information. While the measurement of activation volume at a single stress level may suffice when the relevant obstacle possesses an ideally rectangular force-distance profile [30,32,41], this assumption rarely holds true in practice. Realistic obstacles typically have finite slopes, resulting in an activation volume that is never constant but rather increases as the effective stress decreases [41]. At first glance, this stress-dependence of activation volume seem to render the situation much obscure and incomprehensible. However, it offers a favorable opportunity where the systematic characterization of stress-dependent changes in activation volume can, in fact, unveil the detailed shape of the obstacle profile as an average property throughout the specimen [37,41,52–54]. By applying such an approach to austenitic steels containing solute H, it will be feasible to gain deeper insights into the intrinsic function of H as an impediment element against thermally activated dislocation motion.

As opposed to the short-term (*e.g.*, ~30 s) transient preferred in conventional thermal activation analyses including our foregoing works [10,11], here we utilize a longer-term stress relaxation test extending up to 500–1000 s. This extended timescale enables the relaxation process to cover a broader portion of an entire effective stress spectrum. By analyzing the evolution of relaxation curve as a function of stress-decay, we can derive the stress-activation volume relationship, aligning with the core objectives of our present investigation. The experimental results compellingly reveal a unified stress-dependence of the activation volume between non- and H-charged specimens of the same batch of Type310S austenitic steel studied in our foregoing paper [12]. Ultimately, the finding fundamentally supported the hypothesis we had developed before [10–12], while simultaneously necessitating critical revisions in several key aspects.

2. Methodology

2.1. Material and specimen

A commercial AISI Type310S austenitic stainless steel with a nominal chemical composition of Fe–24.17Cr–19.11Ni–1.11Mn–0.28Si–0.02C–0.031P–0.001S (mass%) was employed in this study. A rod with a diameter of 20 mm was solution-treated at 1353 K for 600 s, followed by water quenching, resulting in a randomly oriented equiaxed grain structure with an average grain size of approximately 50 µm, excluding annealing twins (Fig. 1 (a)). Cylindrical tensile specimens with a gauge diameter of 4 mm and a gauge length of 30 mm (Fig. 1 (b)) were machined from the center of the rod. The gauge surfaces were

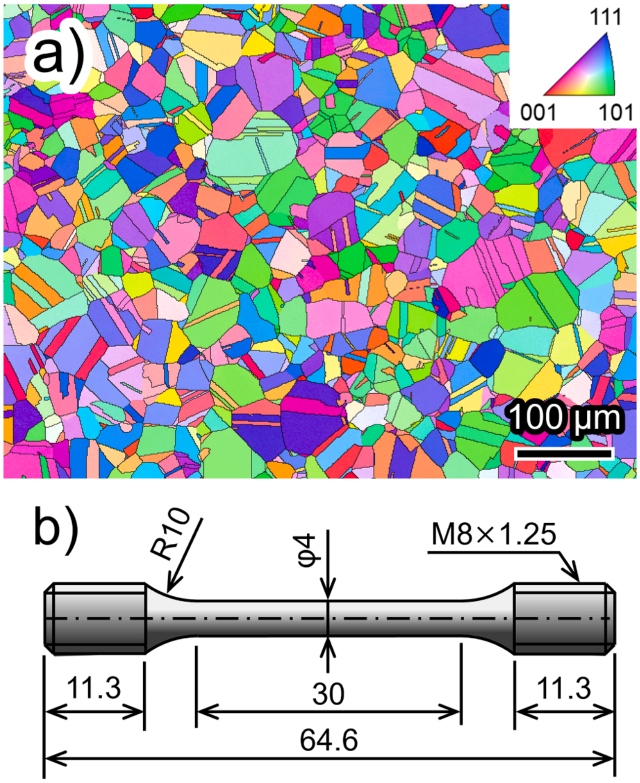

Fig. 1. (a) Microstructure of Type310S steel captured by EBSD on the plane perpendicular to the rod-axis. (b) Shape and dimensions of tensile specimens.

subsequently mirror-polished using a 1 μm diamond suspension.

2.2. H-charging method and H concentration

Tensile specimens were thermally pre-charged with solute H by exposure to high-purity (99.999%) H_2 gas at 543 K for 200 hours in an autoclave. Based on the estimated diffusion coefficient of H in Type310S steel at this temperature ($\approx 1.0\times10^{-11}$ m^2/s [24]), the charging duration was sufficient to establish an approximately uniform H distribution within the gauge sections of the specimens [55]. To vary the solute H concentration, two charging pressures—10 MPa and 100 MPa—were employed. Note that holding the samples at the above charging temperature and time does not affect the mechanical behavior of the present steel as confirmed in our previous study [12].

Following mechanical testing, cylindrical samples 4 mm in length were extracted from the gauge parts of the deformed specimens. Residual H concentrations were quantified using thermal desorption analysis (TDA) with a quadrupole mass spectrometer (HTDS-004, R-DEC, Japan) under a temperature ramp rate of 100 K/h and a range of 298–1073 K. H-charging at 10 and 100 MPa resulted in concentrations of 2400 at ppm (44 mass ppm) and 8500 at ppm (156 mass ppm), respectively, significantly exceeding the baseline concentration of 200 at ppm (3.3 mass ppm) observed in the non-charged specimen. The details of H-desorption spectra are shown in Appendix A1.

2.3. Mechanical tests

Tensile tests, both with and without interruptions by intermittent stress relaxation, were conducted at room temperature (295±2 K) using a screw-driven electromechanical testing machine with a 20 kN load capacity (Shimadzu, AGX-V2). Tensile deformation was applied at a constant crosshead speed of 0.003 mm/s, corresponding to an initial strain rate of 10^{-4}/s. Considering the dimensional tolerance and the resolution of the load cell, the accuracy of stress in the present experiments was within ±1% of the indicated values. Strain was measured using a contact-type strain gauge extensometer with a gauge length of 25 mm, mounted on the specimen during each test.

In the stress relaxation phases, the crosshead was held stationary for 1000 s at selected strain levels, followed by unloading and subsequent reloading toward the next targeted strain. The comparison of relaxation behavior in non- and H-charged specimens was made at a same macroscopic strain to examine the influences of H and stress at a similar internal microstructure. The objective of unloading is the isolation of stress components, the results of which will be presented in our forthcoming paper. Throughout this study, the strain rate applied prior to and in between every “crosshead-holding + unloading” period is referred to as the base strain rate (BSR).

Two specimens were examined for each H concentration to check the generality of the observed H-effects. Relaxation measurements were conducted at nominal strains of 2, 6, 10, 14, 18, 22, 26, 30, and 34% (true strains of 0.02, 0.06, 0.10, 0.13, 0.17, 0.20, 0.23, 0.26, and 0.29) in the first set of specimens, while these strains were 4, 8, 12, 16, 20, 24, 28, and 32% in the second set. In the following sections, only the results from the former are shown for simplicity, since the trends were the same even in the latter (Appendix A2). For non-charged specimens, additional tests were conducted at faster BSRs of 10^{-3}/s and 10^{-2}/s. The relaxation due to the flexure of the testing machine [56] was also evaluated, confirming that its influence is insignificant (Appendix A3).

In the case of prolonged mechanical transients, phenomena other than thermally activated overcoming of short-range obstacles may intervene. A representative example is strain-aging, which arises from the diffusion of interstitial carbon and strain-induced vacancies [45,57,58], potentially retarding the stress relaxation rate and altering the activation parameters. To exclude and assess the influence of this secondary effect, supplemental static strain-aging tests were conducted using non-charged specimens. The specimens were initially deformed at a BSR of 10^{-4}/s and then partially unloaded by 50 MPa in normal stress upon reaching predetermined strain levels. Following this unloading, the crosshead of the testing machine was held stationary for a specified duration—10, 100, or 1000 s—before reloading. The re-yielding behavior during this reloading phase was evaluated to quantify the strain-aging effects.

3. Theoretical background

3.1. Physical description of thermally activated deformation

The kinetics of plasticity governed by dislocation motion through a field of short-range obstacles on the slip plane can be described by an Arrhenius-type rate equation [30,32,33,41,42]:

$$\dot{\gamma} = \dot{\gamma}_0 \exp\left(-\frac{\Delta G}{kT}\right) \tag{1}$$

where $\dot{\gamma}$ is shear strain rate, ΔG is the Gibbs free energy required for a dislocation to overcome an obstacle *via* thermal activation, k is Boltzmann's constant, and T is absolute temperature. The pre-exponential factor, $\dot{\gamma}_0$, is given by the product of mobile dislocation density, ρ_m, average spacing between dispersed obstacles, and vibrational frequency of dislocation line. ΔG can be expressed as a function of the zero-stress activation energy, ΔG_0 , the effective shear stress, τ^*, and the activation volume, V:

$$\Delta G = \Delta G_0 - \tau^* V \tag{2}$$

Geometrically, V corresponds to the area swept by a dislocation segment during each elementary thermal activation event (activation area, A), multiplied by the Burgers vector, $b = 2.5\times10^{-10}$ m. It is expressed as $V = bA = bdL$, where d is an effective obstacle width, and L is the length of the dislocation segment involved in an activation event [41]. From eq. (2), it follows that:

$$V = -\left.\frac{\partial \Delta G}{\partial \tau^*}\right|_T \tag{3}$$

Differentiating eq. (1) with respect to τ^* and applying eq. (3), one can obtain:

$$\frac{kT}{V} = \frac{\partial \tau^*}{\partial \ln\dot{\gamma}} = \frac{\partial \tau}{\partial \ln\dot{\gamma}} \tag{4}$$

The parameter defined by eq. (4) is called strain rate sensitivity. Here, τ is the externally applied shear stress consisting of internal stress, τ_μ, and τ^* ($\tau = \tau_\mu + \tau^*$).

During stress relaxation under a fixed machine crosshead, elastic strain stored in the specimen-machine assembly with an overall elastic stiffness, E, is progressively replaced by plastic strain in the specimen's gauge part. From a macroscopic perspective, the strain rate due to thermally activated plasticity (eq. (1)) can thus be expressed as [56,59]:

$$\dot{\gamma} = -\dot{\tau}/E \tag{5}$$

where $\dot{\tau}$ is the drop rate of shear stress (a negative quantity). In this study, experimentally measured normal stress and strain were converted into shear form as appropriate, considering the average Taylor factor of $M = 3.06$ for polycrystalline FCC materials.

3.2. Experimental determination of activation volume

In metallic materials, stress relaxation typically follows a logarithmic dependence on time, t. The activation volume, V, is commonly evaluated by fitting experimentally obtained relaxation curves using the following equation [30,48,56,59,60]:

$$\Delta\tau = \frac{\Delta\sigma}{M} = -\frac{kT}{V}\ln\left(\frac{t}{c_r} + 1\right) \tag{6}$$

$\Delta\tau$ and $\Delta\sigma$ (both negative quantities) represent the reductions in shear and normal stress, respectively, from their initial values at the start of relaxation. c_r denotes a fitting parameter involving E and V [36,48]. Eq. (6) assumes a constant value of V, a valid approximation for short relaxation times (*e.g.*, 30 s) and small variations in stress, strain and mobile dislocation density. However, the premise breaks down for longer relaxations (*e.g.*, > 100 s), where significant changes in those variables arise. This urges us to use another approach to determine V at any arbitrary moment during the relaxation process.

Differentiating eq. (6) with respect to time and incorporating eq. (5) yields:

$$\frac{\partial\tau}{\partial t} = -\frac{kT}{V}\frac{1}{c_r + t} = -E\dot{\gamma} \tag{7}$$

Taking the logarithm of both sides and time-differentiating again, eq. (7) becomes:

$$\frac{\partial \ln(\dot{\gamma})}{\partial t} = -\frac{1}{t + c_r} \tag{8}$$

By combining eqs. (5), (7), and (8), we arrive at the following expression [30]:

$$V = kT\frac{\partial \ln(\dot{\gamma})}{\partial \tau} = kT\frac{\partial \ln\left(-\frac{\dot{\tau}}{E}\right)}{\partial \tau}$$

$$= kT\frac{\partial \ln(-\dot{\sigma}/ME)}{\partial \sigma/M} = MkT\frac{\partial \ln(-\dot{\sigma})}{\partial \sigma} \tag{9}$$

where σ and $\dot{\sigma}$ denote normal stress and its drop rate, both can be measured directly in the experiments. Eq. (9) thus provides a practical method to evaluate V at any point during the relaxation by plotting $\ln(-\dot{\sigma})$ against σ and extracting the local slope. In this case, the influences from the changes in stress, strain, and mobile dislocation density during the relaxation can be minimized since the V is determined from a short segment (*i.e.*, narrow stress range) of the relaxation curve. The use of such a form of plot (or $\ln(-\dot{\sigma})$ vs. $\ln\sigma$) was proposed by Guiu and Pratt [56], later applied to various FCC materials including Cu [54,61], Al alloys [62], α-brass [63], and Fe-Ni [64]. One can notice that eq. (9) can also be yielded by plugging eq. (5) into eq. (4). Physically, our procedure is equivalent to performing a series of experiments in which a number of specimens are deformed to a target strain and then subjected to short-term stress relaxation to determine V, each conducted at a different BSR. Because the flow stress at the onset of relaxation in such tests depends on the preceding BSR, a similar relationship between V and stress would be obtained.

It should be noted that the V measured in this study inherently includes the influence of secondary phenomena such as strain-hardening during stress relaxation, and hence V should more appropriately be referred to as an apparent activation volume [48]. Nevertheless, these factors do not affect the essential results presented in this work. Further details regarding the possible influence of such secondary factors are provided in Appendix A4.

4. Results

4.1. Escalation of flow stress after H-charging

Fig. 2 shows the true stress–true strain and strain-hardening rate curves obtained from monotonic tensile tests conducted on non-charged and H-charged specimens with three distinct H concentrations, performed at a strain rate of 10^{-4}/s and a temperature of 295 K. As the H concentration increases, the stress–strain curves exhibit an approximately parallel upward shift toward higher stress levels. This parallel shift is an indication of the H-induced solid solution-hardening [11,22,23], wherein H hinders the motion of individual dislocations with its insignificant effect on the development process of dislocation structures [10,12,65]. In other words, H-induced resistance to dislocation motion acted additively to the intrinsic strain-hardening of the material, making the present comparison of stress relaxation behavior at a fixed strain (*i.e.*, under similar dislocation structures irrespective of the presence or absence of H) reasonable. The stress increment was approximately 10–20 MPa and 50 MPa for H concentrations of 2400 and 8500 at ppm, respectively. This behavior is consistent with our previous findings, which demonstrated that the degree of solid solution-hardening is nearly proportional to the H concentration under deformation conditions equivalent to the present case [22,23].

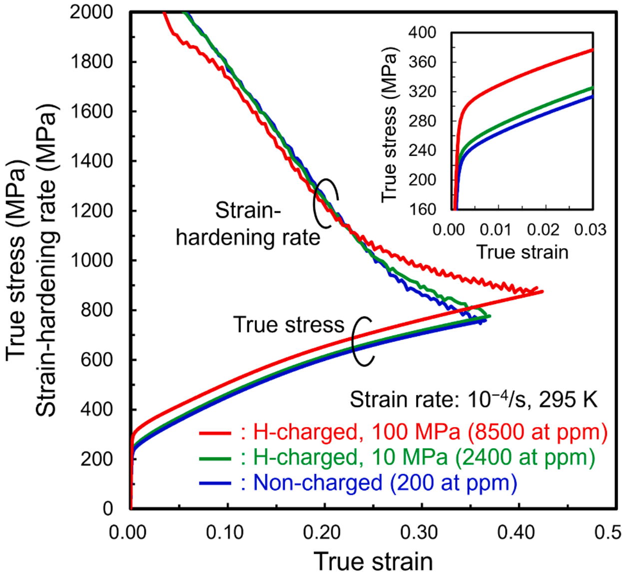

Fig. 2. True stress-strain and strain-hardening rate curves of the non-charged and H-charged specimens with different solute H concentrations, wherein the inset enlarges the regime around their yield stresses.

As a consequence of H-induced solid solution-hardening, the applied stress at the point of test interruption (*i.e.*, when the crosshead was held at a fixed strain) varies depending on the H concentration. In particular, the initial stresses at the onset of stress relaxation were increased by approximately 10–20 MPa and 50 MPa for specimens charged with 2400 and 8500 at ppm H, respectively, relative to the non-charged specimen.

4.2. Stress relaxation behavior

The stress relaxation curves ($\Delta\sigma$ vs. time) at representative strain levels for non- and H-charged specimens are presented in Fig. 3, where the stress at the onset of relaxation was set to zero. Fig. 3 (a-1), (b-1), and (c-1) highlight the initial 30 s, whereas Fig. 3 (a-2), (b-2), and (c-2) extend the time window to 400 s. Beyond this range, especially after 500 s, relaxation became too slow—particularly in the non-charged specimen—for reliable quantification of the relaxation rate. Accordingly, the following analysis focuses on data within the first 400–500 s. Due to the higher initial stresses at the onset of relaxation, the H-charged specimens exhibited greater stress-drops across all strain levels, the effect particularly pronounced at the H concentration of 8500 at ppm. This trend aligns with our previous findings [10,11], which suggest that H-induced solid solution-hardening primarily originates from an increase in effective stress. In other words, the greater relaxation magnitude in H-charged specimens reflects the decay of these additional effective stresses with the aid of time.

In the non-charged specimen, the magnitude of stress relaxation increased consistently with pre-relaxation strain (Fig. 3 (a)). A similar strain-dependence was observed in the H-charged specimen containing 2400 at ppm H (Fig. 3 (b)). In contrast, such dependence was largely

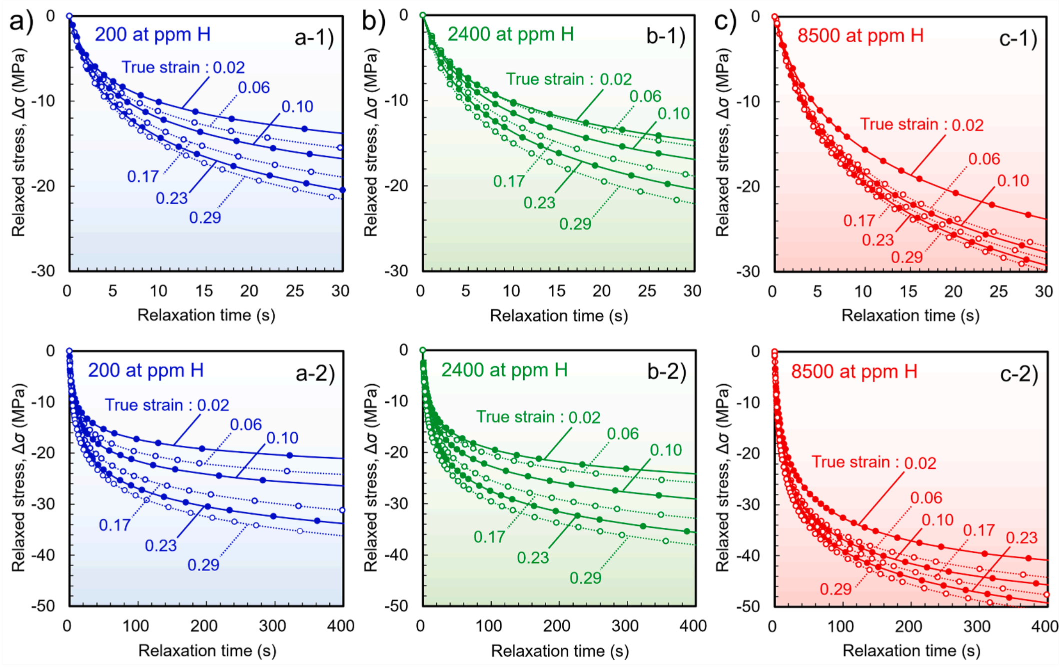

Fig. 3. Stress relaxation curves (*i.e.*, stress decay vs. time) in the specimens containing (a) 200, (b) 2400, and (c) 8500 at ppm H, measured at various strain levels under 295 K and a base strain rate of 10^{-4}/s. (a-1), (b-1), and (c-1) present the initial stage of relaxation until 30 s, while (a-2), (b-2), and (c-2) extend the time frame up to 400 s.

absent during the initial ~10 seconds in the specimen charged with 8500 at ppm H, particularly at strains exceeding 0.06 (Fig. 3 (c-1)). However, after 10 seconds, relaxation in this specimen also became strain-dependent (Fig. 3 (c-2)), albeit to a lesser extent compared to the other two specimens.

4.3. *Transition of relaxation curve*

According to eq. (9), the $\ln(-\dot{\sigma})$ vs. σ relationships were derived by taking time derivatives of the relaxation curves shown in Fig. 3 and represented in Fig. 4. For a constant value of V, this $\ln(-\dot{\sigma})$–σ curve should be a straight line that was assumed in eq. (6). However, except for the beginning relaxation stage, these curves in Fig. 4 were far from such linearity but rather exhibited an increasing slope with the progress

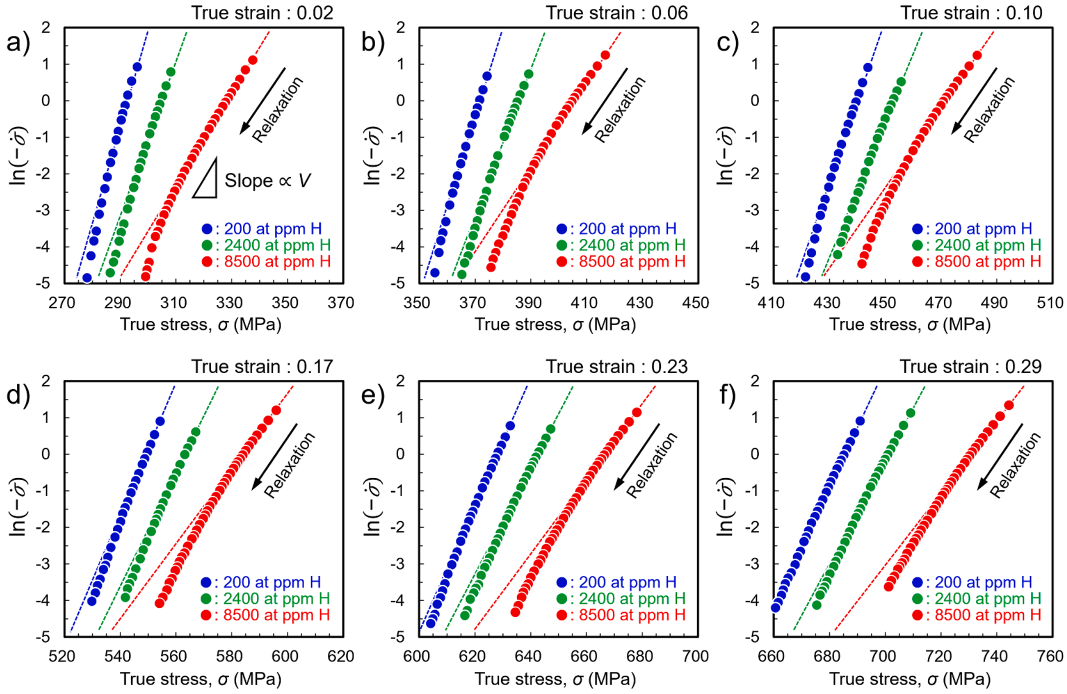

Fig. 4. Reproduction of the stress relaxation curves in Fig. 3 in the form of $\ln(-\dot{\sigma})$–σ. The absolute values of stress, σ, is used for abscissa instead of the drop from their initial values, $\Delta\sigma$ (Fig. 3). (a)–(f) denote the behavior at different strain levels.

of relaxation (arrows in Fig. 4) and corresponding decrease in applied stress. The slope change indicates the stress-dependence of V as mentioned in Section 1. The $\ln(-\dot{\sigma})$–σ slope was smaller in H-charged specimens, particularly when the applied stress was high. This smaller slope signifies the reduction in V due to H-charging, reproducing the facts found in the previous investigations by authors [10,11,55] and other researchers [6,66,67].

To compare the stress-dependent law of relaxation, an offset along $\ln(-\dot{\sigma})$-axis was implemented into Fig. 4. Namely, $\ln(-\dot{\sigma})$–σ curves of the non-charged specimen and the H-charged specimen with 2400 at ppm H were displaced downward so that their curves visually converge into the specimen with 8500 at ppm H (see the inset of Fig. 5). As its physical meaning will later be described in Section 4.4 and Section 5.3.3, the magnitudes of these offsets reflect the differences in the relaxation strain rate between non-charged and H-charged specimens. The results are depicted in Fig. 5 where the flow stresses (*i.e.*, the stresses at the start of relaxation) in the H-charged specimen with 8500 at ppm were set to zero for clarity. Some examples of the offset values are indicated in brackets. Impressively, at all strain levels, the $\ln(-\dot{\sigma})$–σ under three different H concentrations converged into unified master curves, exhibiting a continuous increase in its slope with a decrease in stress. The master curves had an almost identical slope at the high stress regime of $\Delta\sigma = -20$–0 MPa, corresponding to the weaker strain-dependence of relaxation behavior in Fig. 3 (c-1). Then, they diverged with diminishing their curvature as the pre-strain before relaxation was increased.

4.4. *Stress-dependences of activation volume and deformation kinetics*

From the unified law of $\ln(-\dot{\sigma})$–σ in Fig. 5, the corresponding V also requisitely leads to a unified stress-dependence irrespective of the presence and absence of H. Fig. 6 proves it for various strain levels by calculating the master curve slopes in Fig. 5 (equivalent to calculating the slopes of $\ln(-\dot{\sigma})$–σ curves in Fig. 4) and employing eq. (9). Obviously, V continuously became larger with the decrease in stress, initially lying around $80b^3$ and escalating over $150b^3$.

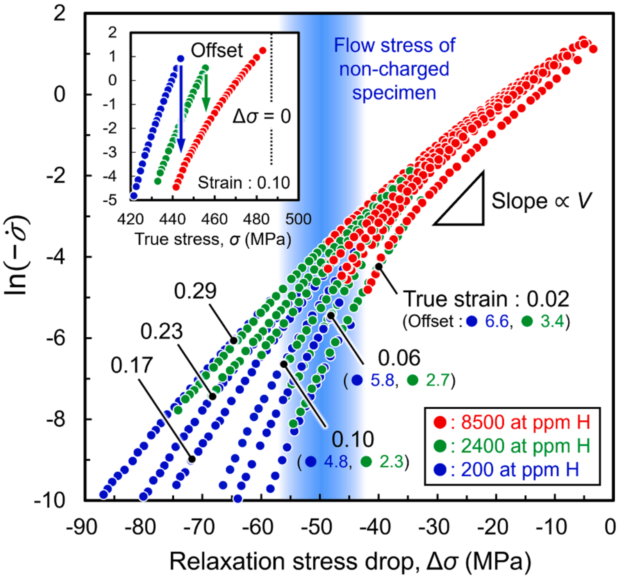

Fig. 5. Revision of Fig. 4 to demonstrate the continuity in $\ln(-\dot{\sigma})$–σ trend. The curve for each strain was constructed by negatively offsetting the curves at 200 and 2400 at ppm H along the vertical axis so that they merge into that of the 8500 at ppm H specimen (some examples of offset values are indicated in the brackets). For converging all master curves close to each other, stresses at the start of relaxations under 8500 at ppm H were set to zero. An example of these procedures is shown in the inset.

Based on eq. (5), the plastic strain rate during the stress relaxations in Fig. 3 was estimated and represented in Fig. 7. Here, normal stress-strain was used instead of their shear counterparts (eq. (5)), and the stiffness of the specimen-machine assembly was approximated by the slope of stress vs. crosshead displacement diagram during the elastically deforming domain before yielding ($E \approx 465$ kN/strain ≈ 37 GPa/strain). The trend of specimen-to-specimen difference in relaxation strain rate was also checked by the extensometer signal (Appendix A5), albeit the small level of relaxation strain made the signals noisier.

In all situations, the strain rates at the beginning of relaxations were close to 10^{-4}/s, *i.e.*, base strain rate (BSR) (see circle plots in Fig. 7), an inevitable consequence due to the deformation continuity before and after the onset of crosshead-holding. Then, the strain rates were exponentially slowed down to $\approx 10^{-7}$/s as the relaxation progressed and stress decreased. The most important observation from Fig. 7 was the orders of magnitude slower strain rate in the H-charged specimens compared to the non-charged specimen when comparison was done at a fixed stress level—for instance, compare the strain rates along the dashed vertical lines, which denote the flow stress levels in the non-charged specimen under BSR $= 10^{-4}$/s. This finding emphasizes that the increasing concentration of solute H retards plastic deformation under a given stress, even though V followed the unified stress-dependent law in both non- and H-charged specimens (Fig. 6). Returning to Section 4.3, the offset of the $\ln(-\dot{\sigma})$–σ curves in Figs. 4 and 5 along their $\ln(-\dot{\sigma})$ axis is equivalent to compensating for these gaps of strain rate since the stress drop rate is a direct function of relaxation strain rate (Eq. (5)). Taking the non-charged specimen as a baseline, the gaps in $\ln(-\dot{\sigma})$ calculated from the offset values are respectively 3.2 and 6.6 for 2400 and 8500 at ppm H at a strain of 0.02. These correspond to 30- and 700-times slower strain rates, for instance.

4.5. *Effects of strain-aging in mechanical transient*

The results of strain-aging tests on non-charged specimens are presented in Fig. 8, with an example of the yielding behavior upon reloading in its inset. When the specimen was plastically deformed again after unloading, minute yield-point was often observed, an indication of strain-aging effects [44,57]. The plots in Fig. 8 summarize the stress gap between prior flow stress and strain-aging-induced yield-point, $\Delta\sigma_{\mathrm{YP}}$, for the aging times of 10, 100, and 1000 s as a function of strain. The significance of $\Delta\sigma_{\mathrm{YP}}$ was minor at smaller strain and shorter aging time but became gradually pronounced as the increases in these two variables (*e.g.*, ≈ 3 MPa by the aging of 1000 s and the strain of 0.3).

5. Discussion

5.1. *Primary finding and its physical significance*

The most significant finding in the present study was *the consistent stress-dependent law of V that holds irrespective of the presence and the concentration of H* (Fig. 6). In all cases employed for the experiments, V monotonically increased with a decrease in stress, converging the V-stress relationships in non- and H-charged specimens under a given strain into an identical master curve. This feature invokes our past discovery wherein one-to-one interrelation between yield stress and corresponding V held under diverse H concentrations [10]. Intuitively, we called it *stress-equivalence* in an analogy with the phrasing used by Basinski et al. [40]. From a macroscopic viewpoint, the continuous variation in V appeared as the progressively downward curvature of the $\ln(-\dot{\sigma})$–σ curves.

The downward curvature of $\ln(-\dot{\sigma})$–σ, as well as some related changes in relaxation behavior, can be encompassed nevertheless by strain-aging [57,63]. In our Type310S steel, durations up to 1000 s yielded considerable $\Delta\sigma_{\mathrm{YP}}$ (Fig. 8) with an increasing extent with strain

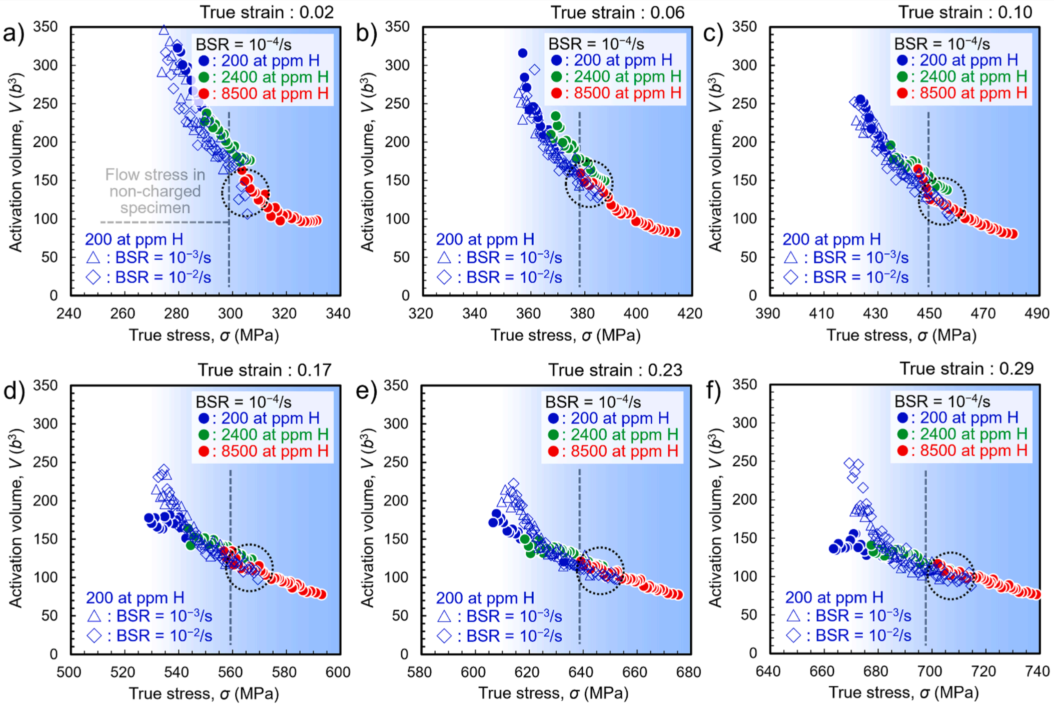

Fig. 6. Stress-dependence of activation volume, V, at representative strain levels. The circle plots provide the effects of H-concentration evaluated at the base strain rate (BSR) of 10^{-4}/s, while blue triangles and diamonds superpose the data of non-charged specimens obtained at BSRs of 10^{-3}/s and 10^{-2}/s, respectively.

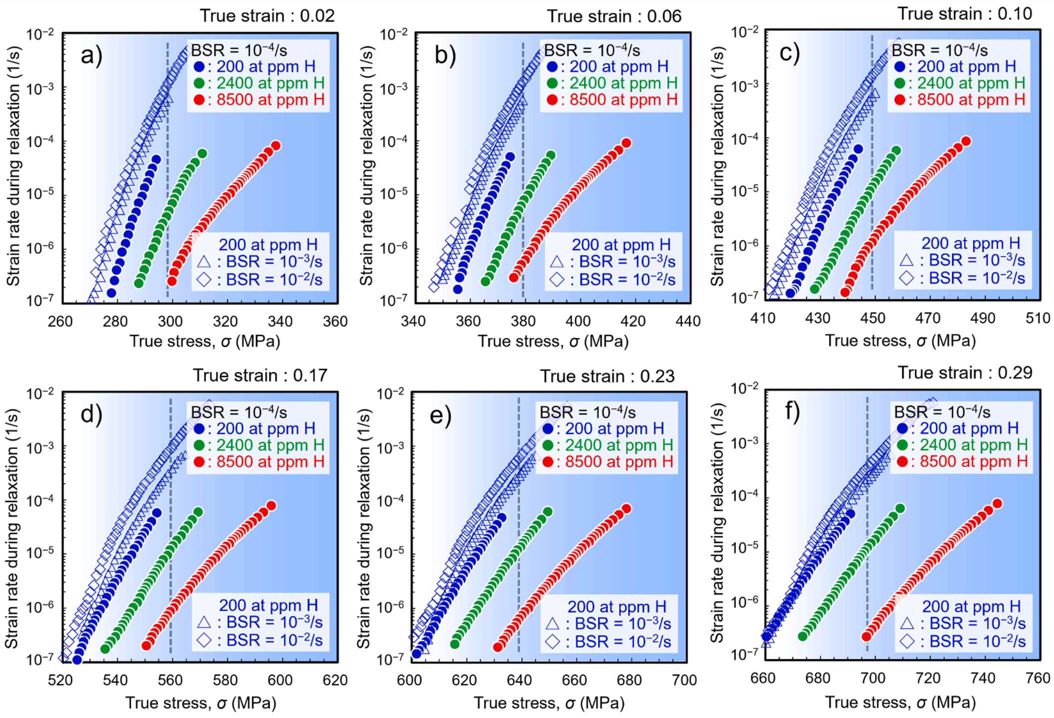

Fig. 7. Stress-dependence of plastic strain rate during relaxations at representative strain levels. The circle plots provide the effects of H-concentration evaluated at base strain rate (BSR) of 10^{-4}/s, while blue triangles and diamonds superpose the data of non-charged specimens obtained at BSR = 10^{-3}/s and 10^{-2}/s, respectively. The dashed vertical lines denote the flow stress of the non-charged specimen at each strain level under BSR = 10^{-4}/s.

and time. A caution thus arises that strain-aging might somewhat impact the present long-term relaxation, while $\Delta\sigma_{YP}$ in aging tests (Fig. 8) were an order of magnitude smaller than $\Delta\sigma$ in stress relaxation tests (Fig. 3). However, the curvature of $\ln(-\dot{\sigma})$–σ readily appeared at strains below 0.10 (Figs. 4 and 5), where the extent of aging was marginal (Fig. 8). Moreover, the $\ln(-\dot{\sigma})$–σ at the later relaxation phase in H-charged specimens exhibited smooth connections to those at the beginning relaxation phase in the non-charged specimen (Fig. 5). These points evidence the physical significance of our key finding in elaborating the latent mechanisms governing thermally activated plasticity, even

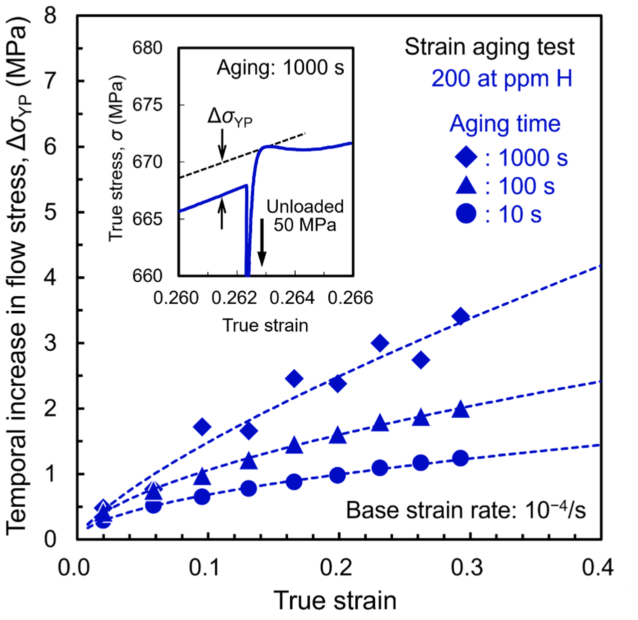

Fig. 8. Results of static strain-aging tests for non-charged specimens, in which partial unloading and subsequent crosshead-holding were implemented at various strains. The inset shows an example of stress-strain responses around these test interruptions.

though aging-effects cannot be disregarded completely.

There is also a possibility that the presence of solute H could have influenced the strain-aging behavior. However, our previous static strain-aging tests for 600 s on H-charged specimens of the same steel [55] have demonstrated that the effect of H at a comparable concentration is negligible. Furthermore, if H was an element that induces aging, dynamic strain-aging would be expected even during deformation. In general, when a diffusive element causes dynamic strain-aging, V tends to increase (*i.e.*, strain rate sensitivity decreases) [43]. However, H caused the opposite tendency. Therefore, in the present study, the extent of strain-aging is considered to be equivalent between the non-charged and H-charged specimens, although the latter was not examined.

5.2. Role of H on the ground of inherent obstacle types

5.2.1. Commonality of obstacle types controlling activation volume

Fig. 9 (a) depicts the force-distance profile commonly used to describe obstacle-dislocation interactions (whatever the obstacle type) [32] under an effective shear stress, τ^* (its normal counterpart is σ^*). According to eq. (2), the total activation energy for overcoming the obstacle, ΔG_0, consists of thermally supplied energy, ΔG, and mechanical work term, $\tau^* V$. Due to the increase/decrease in τ^*, V is varied through the change in effective obstacle width, d [41] (compare Fig. 9 (a-1) to (a-2)). Thus, drawing the stress-V relationship as for Fig. 6 is physically equal to tracing the half-side of the obstacle potential shape in Fig. 9 (a), although the influence of stress-dependent change in the length of activated dislocation segment is also involved in V (later shown in Fig. 10). This is the so-called *glide-resistance diagram* defined by Kocks, Argon, and Ashby (Fig. 9 (b)) [41]. Note, however, that the horizontal and vertical axes are switched with each other in Fig. 6 from the original form in [41].

The V-stress curve of the non-charged specimen in Fig. 6 crops a section of such glide-resistance diagram (solid curve in Fig. 9 (b)) relevant to the short-range obstacles intrinsically contained in the material (*i.e.*, alloying elements and/or forest dislocations). Considering its continuity with the curves of H-charged specimens, it is inferred that stress elevation by solid solution-hardening in H-charged specimens merely uncovers a higher-stress portion of the same glide-resistance diagram intrinsic to the non-charged state (dashed curve in Fig. 9 (b)). A

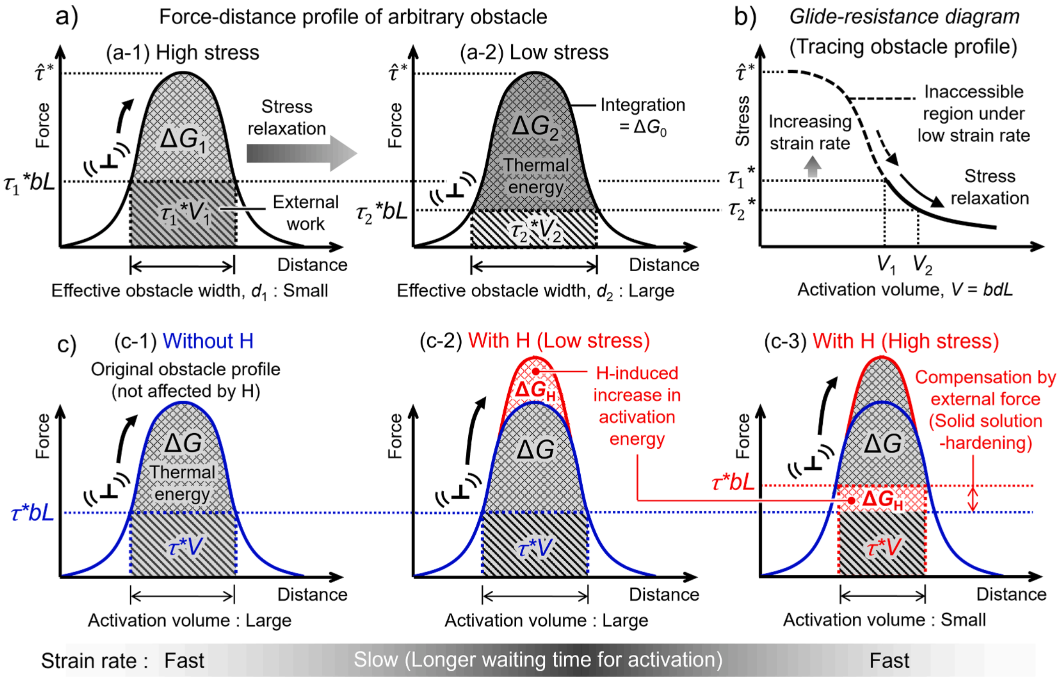

Fig. 9. Schematic force-distance profile of a thermally activatable obstacle interacting with a mobile dislocation. (a) shows the general effects of effective stress on thermal activation energy, ΔG, and activation volume, V, resulting in the *glide-resistance diagram* (*i.e.*, stress vs. V) in (b). (c) describes how solute H virtually changes the glide kinetics by putting an extra activation energy, ΔG_H, atop the original obstacle profile (c-2). Additional mechanical work term to compensate for this ΔG_H (red cross-hatched area in (c-3)) is required for the H-charged specimen to plastically deform at the same rate with the non-charged specimen, resulting in an increase in flow stress (*i.e.*, solid solution-hardening).

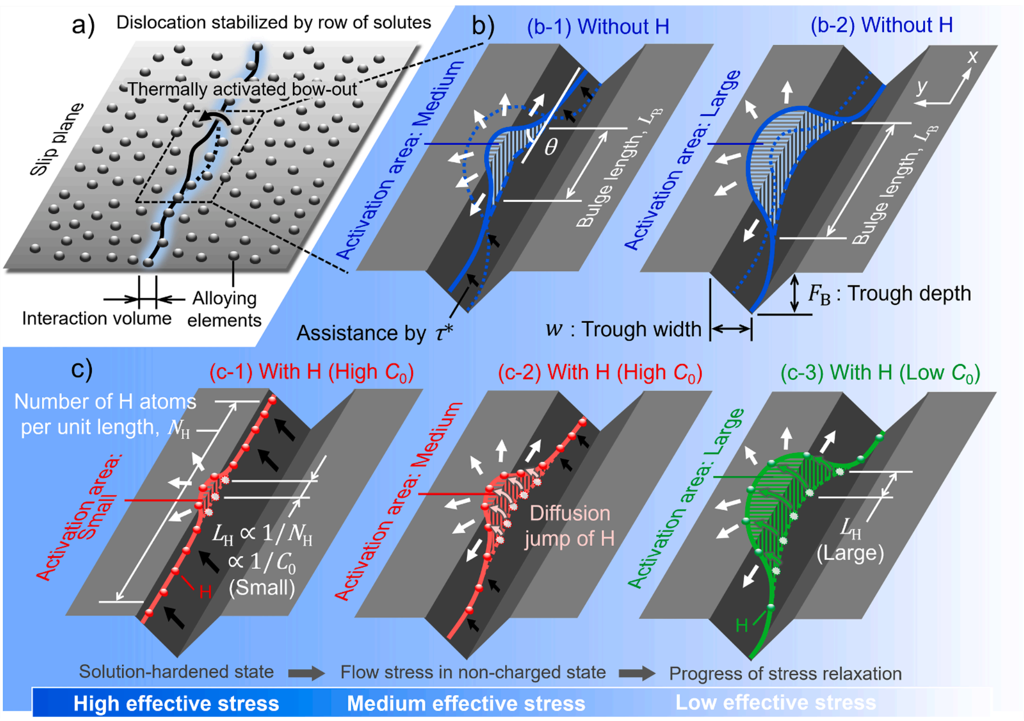

Fig. 10. *Trough model* of solid solution-hardening: (a) dislocation line stabilized by solute atoms attempts to advance *via* bowing out a bulge with the aid of stress and thermal activation. (b) depicts the stress-effects on bulge configuration and corresponding activation area (or activation volume). While solute H does not change the stress-dependence of such activation process, (c) the necessity of their coordinative diffusion jump with the motion of dislocation core potentially retards the critical bulging. The background gradation in (b) and (c) denotes the stress levels indicated by the same colors in Fig. 6 and Fig. 7. (c-1) and (c-2) correspond to the situations shown in Fig. 9 (c-3) and (c-2), respectively. In (b) and (c), the illustrations purposely expanded into the *y*-axis for clarity, although the bulge excursion may occur in an atomic scale in practice.

straightforward verification of this forecast is to measure V in the non-charged specimen under the stresses greater than the range examined up to here. In order to accomplish it, stress relaxation tests with faster base strain rates (BSRs) of 10^{-3}/s and 10^{-2}/s were carried out to access higher flow stresses at the onset of relaxation (dashed arrow in Fig. 9 (b)). The resulting V and relaxation strain rates are superimposed in Fig. 6 and Fig. 7. These tests successfully captured the V-stress curve in the higher stress regime (dotted circles in Fig. 6), previously inaccessible with slower BSRs. Consistent with the forecast, the V–stress curves from these tests aligned with those of H-charged specimens at $\mathrm{BSR} = 10^{-4}$/s. This coincidence leads to a first key conclusion in the present study: *irrespective of the presence and absence of H, V is solely governed by applied stress, emphasizing that solute H does not change the obstacle types controlling V*. At $\mathrm{BSR} = 10^{-3}$/s and 10^{-2}/s, the relaxation strain rates under a given stress were slightly faster than those at $\mathrm{BSR} = 10^{-4}$/s, though the gaps remained relatively small (Fig. 7).

In Fig. 6, the results for the non-charged specimens measured at different BSRs notably converged onto a single curve especially at low to moderate strain (Fig. 6 (a-c)). This validates our premise made in Section 3.2 that “our procedure is equivalent to performing a series of experiments in which number of specimens are deformed to a target strain and then subjected to short-term stress relaxation to determine V, each conducted at a different BSR”. If the V determined from any arbitral parts of relaxation curve could be affected by prior deformation history or time, such a consistency would not hold.

5.2.2. Extra glide activation barrier supplied by H

While the obstacle nature determining V was not altered by H, another notable aspect was the orders of magnitude slower relaxation strain rates in H-charged specimens under a given stress and fixed V (Figs. 6 and 7). This lower strain rate means a delay and more viscous progress of thermally activated deformation, reproducing our foregoing finding on the suppression of room temperature creep when pre-deformed non- and H-charged specimens were subjected to an identical stress [12]. Referring to eq. (1), it implies either a reduced $\dot{\gamma}_0$ or an increased ΔG.

A smaller $\dot{\gamma}_0$ can be attributed to a reduced mobile dislocation density, ρ_m, assuming constant obstacle interspacing—a valid assumption since H does not alter obstacle properties (Fig. 6). Before stress relaxation, both non- and H-charged specimens should possess similar ρ_m to accommodate the same externally imposed strain rate, as supported by the negligible H effect on strain-hardening rate in Type310S steel in low-to-medium strain regime where plasticity is solely carried by dislocations [10,55]. Mobile dislocations are gradually trapped into organized dislocation structures (*e.g.*, walls, cells), contributing to strain-hardening [68–70], thereby any significant H-induced change in ρ_m would manifest as altered strain-hardening behavior—which has not been observed. Our *in-situ* neutron diffraction study on the same steel further confirmed that dislocation density evolution is unaffected by H [65]. Although stress relaxation reduces ρ_m *via* dislocation storage and annihilation, FCC metals can retain a significant fraction of ρ_m even after hundreds of seconds [30,60,71]. Thus, the large difference in relaxation strain rate (Fig. 7) cannot be explained solely by variations in ρ_m. Indeed, conventional thermal activation analyses typically disregard ρ_m due to the more dominant influence of the exponential term in eq. (1) [41].

Given that the difference in $\dot{\gamma}_0$ is not a primary reason, the only factor that can significantly retard the relaxation strain rate is the increase in ΔG due to H. This view aligns with the recent crystal plasticity simulation stated that the increase in glide activation energy is the sole explanation for the H-induced hardening in austenitic stainless steels [72]. Fig. 9 (c) schematically describes how H might affect the original obstacle profile in Fig. 9 (a). Considering the unified V-stress curves (Fig. 6) restricting the mountainsides of the original profile (Fig. 9 (a)) to be unchanged, we reach the second key conclusion: *the impact of H can be accounted as virtually putting an extra glide activation energy, ΔG_H, atop the original obstacle profile* whatever its potential shape is (Fig. 9 (c-2)). The presence of ΔG_H under a fixed stress requires a larger thermal energy to be supplied with the aid of time, prolonging the waiting time for dislocation to overcome individual obstacles. In other words, for forcibly progressing the deformation with the same rate with the non-charged case, H-charged specimens need additional mechanical work to compensate for ΔG_H (red hatched area in Fig. 9 (c-3)). Exactly, the effective stress to create this extra mechanical work is the origin of H-induced solid solution-hardening under a fixed strain rate (Fig. 2). Thanks to such an escalated stress, an access to more upper portions of the *glide-resistance diagram* in Fig. 9 (b) became feasible, yielding the smaller V as a matter of necessity.

The illustration in Fig. 9 (c-2) now urges us to revisit our previous concept—H atoms act as short-range obstacles with more localized and thermally activatable characteristics and may be promoted into primary rate-controlling obstacles as alternative to other inherent obstacles—reiterated in [10–12] and Section 1. This statement is partially valid because H supplies additional energy barrier, ΔG_H, which can be thermally overcome by a prolonged waiting time. However, the invariance of V-stress curves in Fig. 6, *i.e.*, *glide-resistance diagram* in Fig. 9 (b), demonstrates that the primary obstacles resisting the dislocation glide are still the inherent ones originally involved in the material (*i.e.*, alloying elements and forest dislocations). Rather, the role of H is to hinder the dislocation from surmounting these inherent obstacles by virtually placing an extra hurdle, ΔG_H.

In Section 5.3, we first describe a suitable model of dislocation motion with a special focus on the ground of concentrated alloying elements including Cr, Ni, Mn, and Si, etc. (*i.e.*, the obstacle profile shown in Fig. 9 (c-1) now corresponds to these alloying elements), then attempt to refine and incorporate our H-dislocation interaction model [10,12]. Whereas forest dislocations do contribute to the deformation kinetics [33,38,41], their competitive relationship with these alloying elements will be highlighted in our forthcoming paper.

5.3. A model of dislocation motion interacting with both alloying elements and H

5.3.1. Dislocation motion in concentrated solid solution

Given the high concentrations of Cr, Ni, and other alloying elements in Type310S steel, the conventional solute–dislocation interaction model for dilute alloys—where dislocations are impeded by point-like solute atoms [32,73]—is not applicable. In fact, the solid solution-hardening in austenitic steels containing substitutional solutes with at% levels exhibits a linear dependence on solute concentration, c [13], deviating from the trend proportional to $c^{1/2}$ predicted by point-like approximations [32,73]. Similarly, our results show that H-induced solid solution-hardening follows a linear dependence on H concentration [22,23]. This behavior, along with the distinct role of H discussed in Section 5.2, is not anticipated if H atoms behave as point-like obstacles.

The large V of $>100b^3$ (Fig. 6), typical of dislocation interactions with concentrated solutes [33,40,74], suggests that multiple solute atoms participate in each thermal activation event [40]. A plausible mechanism was first proposed by Feltham [75] and later developed into the *trough model* by Kocks [76]. In Kocks's model (Fig. 10 (a) and (b)), a mobile dislocation aligns along a row of solute atoms (Fig. 10 (a)), which are assumed to be averaged along the dislocation line. The dislocation advances by bowing out a short bulge under the combined action of applied stress and thermal activation. The initial dislocation position corresponds to a potential trough (Fig. 10 (b)), whose depth depends on both the dislocation's binding energy with individual solutes, E_B, and the linear solute density along dislocation line. The solid solution-hardening proportional to average solute concentration is thus reasonable, as the dislocation line takes lowest energy configuration by accommodating randomly distributed solutes within its cylindrical interaction volume (Fig. 10 (a)) [76].

By analogy with the Fisher-type breakaway from the pinning by a row of solute [77] (*i.e.*, assuming a triangular potential well), the activation energy for bulge nucleation [41,76] is given by:

$$\Delta G = \mu b^3 \Psi \sqrt{f_B}\,\frac{1}{S}\sqrt{1-S} \approx \mu b^3 \Psi \sqrt{f_B}\,\frac{1}{S}(1-S) \tag{10}$$

where μ is shear modulus. Ψ, f_B, and S are normalized parameters respectively characterizing the dislocation line energy, solute-dislocation binding energy, and stress that are expressed as follows [76].

$$\Psi = \frac{4}{3}\left(\frac{2F_D}{\mu b^2}\right)^{1/2}\left(\frac{w}{b}\right)^{3/2} \tag{10a}$$

$$f_B = \frac{F_B}{\mu b w} \tag{10b}$$

$$S = \frac{\tau^*}{\mu f_B} \tag{10c}$$

In eqs. (10.a)−(10.c), F_D is line energy of free dislocation, w is trough width (Fig. 10 (b)), and F_B is binding energy of solutes per unit dislocation length.

The approximation $\sqrt{1-S} \approx 1{-}S$ in eq. (10) is valid when the effective stress, τ^*, is well below the obstacle profile peak, $\hat{\tau}^*$, in Fig. 9 (a), as is the case here. Indeed, the yield stress of Type310S steel at 77 K measured under a comparable strain rate [78] is more than doubles that at room temperature [78]. This difference indicates that the effective stress at 295 K lies, at a maximum, in the lower half of the obstacle potential barrier in Fig. 9 (a). Applying the physical definition of V (eq. (3)) and roughly approximating that $F_D \approx \mu b^2/2$ and $w \approx 3b$ [76], eq. (10) becomes:

$$V = -\frac{\partial \Delta G}{\partial \tau^*} = \frac{b^3 \Psi}{\sqrt{f_B}}\frac{1}{S^2} = 4\sqrt{3}\,\frac{b^3}{\sqrt{f_B}}\left(\frac{\mu f_B}{\tau^*}\right)^2 \tag{11}$$

$$\tau^* = \frac{\sigma^*}{M} = \mu f_B\left(\frac{4}{3}\,\frac{b^3 3^{3/2}}{\sqrt{f_B}}\right)^{1/2}\frac{1}{\sqrt{V}} = \left(4\sqrt{3}\,\mu^2 b^3 f_B^{3/2}\right)^{1/2}\frac{1}{\sqrt{V}} \tag{12}$$

If the *trough model* holds, eq. (12) predicts the proportional relationship between stress and $1/\sqrt{V}$ with a slope of $(4{\bullet}3^{1/2}\mu^2 b^3 f_B^{3/2})^{1/2}$. Such stress-induced decrease in V reflects a shortening of the bulge length, L_B, and a reduced forward excursion of the bulge [41] (compare Fig. 10 (b-1) to (b-2)).

Fig. 11 reproduces Fig. 6 in the form of applied stresses in non- and H-charged specimens as a function of $1/\sqrt{V}$ at different strain levels. As anticipated, the data obeys $\sigma \propto 1/\sqrt{V}$ trend up to a strain of 0.10 (Fig. 11 (a)–(c)). Beyond this strain, systematic downward deviations from the proportionality emerged (Fig. 11 (d)–(f)). This deviation is likely due to increasing contributions from forest dislocations, while their impact remains small at lower strain levels.

From Fig. 11 (a)–(c), the slopes of these $\sigma \propto 1/\sqrt{V}$ lines were determined to be $\sigma V^{1/2} \approx 1000$ MPa$\bullet b^{3/2}$ and $\tau V^{1/2} \approx 330$ MPa$\bullet b^{3/2}$. Thus, using the Burgers vector of a perfect dislocation in Fe-Cr-Ni austenitic steels ($b \approx 2.5\times10^{-10}$ m), $\tau V^{1/2} \approx 1.3\times10^{-6}$ N$\bullet$m$^{1/2}$. Comparing such experimental slope with $(4{\bullet}3^{1/2}\mu^2 b^3 f_B^{3/2})^{1/2}$ in Eq. (12), we reach the normalized solute-dislocation binding energy of $f_B \approx 5.4\times10^{-4}$. This value enables us to quantify ΔG as a function of normalized stress, S, by plugging it into Eq. (10). The result of such quantification is presented in Fig. 12. Reasonable values of ΔG were obtained at $S > 0.2$, considering that the maximum energy supplied by thermal vibration is usually less than $20kT$ (≈ 0.5 eV at 295 K) [30]. The range of $\Delta G < 20kT$ sufficiently covers the stress levels of $S \leq 0.5$, where the linear approximation of $\sqrt{1-S} \approx 1{-}S$ in Eq. (10) holds [76]. The activation energy for dislocation glide through matrix frictional resistance in Type310S steel has

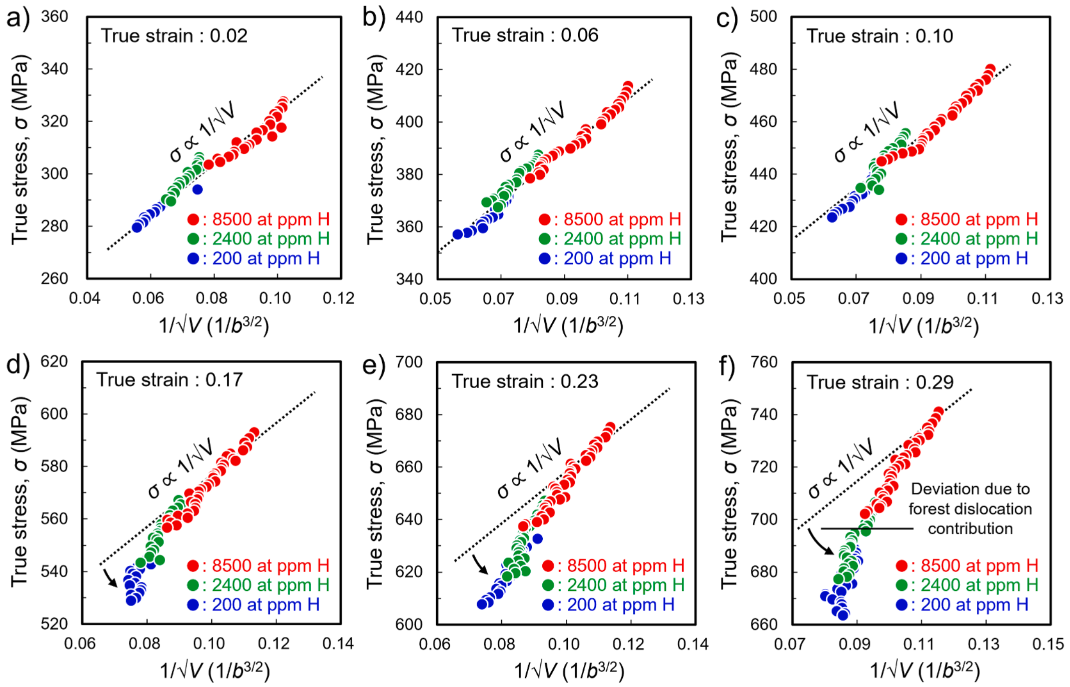

Fig. 11. Stress-dependent law of activation volume, V, at various strain levels. During small-to-intermediate strains up to 0.10, the curves in both non- and H-charged specimens obey $\sigma \propto 1/\sqrt{V}$, implying the applicability of *trough model* to the present material and deformation conditions on the basis of eq. (11) and (12). The arrows in (d)–(f) denote the deviation from such $\sigma \propto 1/\sqrt{V}$ law possibly due to the forest dislocation contributions.

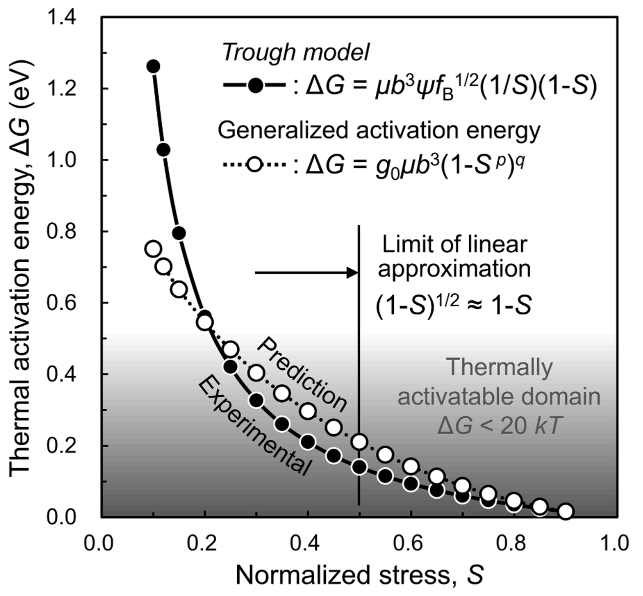

Fig. 12. Stress-dependent variation of activation energy, ΔG, calculated by eq. (10) using the $\sigma \propto 1/\sqrt{V}$ relationship in Fig. 11 (a)–(c) (solid marks). The literature data of glide activation energy in the same steel [78] based on eq. (13) is included for comparison (open marks).

also been evaluated by Tsuchida et al. for the deformation temperature range between 77–296 K [78]. They employed a more general form of ΔG [79]:

$$\Delta G = g_0 \mu b^3 (1 - S^p)^q \tag{13}$$

where g_0 was experimentally determined to be 0.17 and the general values of exponents were used as $p = 0.5$ and $q = 1.5$ [30,41]. In Fig. 12, the ΔG–S curve predicted by their data is included for validating our experimental parameterization. A fair agreement between the two curves is evident, except for the deviation at $S < 0.2$. This coincidence notably verifies the adequacy of adopting *trough model* into the present Type310S steel unless the stress level is too low. In other words, it demonstrates a certain and primary contribution of alloying elements to thermally activated plasticity in the present experiments.

5.3.2. *Potential form of H-induced glide resistance*

To incorporate the role of H into the *trough model* (Fig. 10), it is essential to consider dynamic interactions between mobile dislocations and diffusible H [2,4,5,8,80–82]. Attractive interactions between H and dislocations lead to H segregation along dislocation cores and the formation of H atmospheres within their elastic stress fields [8,23,83–86]. When favorable combinations of strain rate and temperature are met, these atmospheres can coordinatively migrate with dislocations [80,82, 83]. At first glance, this coordinated motion is thought to enhance f_B in eq. (10)—deepen the trough in Fig. 10 (b)—as theoretical formulations suggest that H atmospheres reduce the dislocation line energy or line tension [87,88]. However, if f_B was modified, the $\sigma \propto 1/\sqrt{V}$ slopes would differ between non- and H-charged specimens, which was not the case in Fig. 11.

Using the numerical framework by Sills et al. [82,83], we evaluated the ability of H to follow moving dislocations [11,23], employing experimentally determined H diffusivity [26] and swelling volume per H atom [84,89] in Type310S steel. Under post-yield conditions, where mobile dislocation density exceeds $10^{13}/\text{m}^2$ [70,90] and tensile strain rate is below 10^{-4}/s, our calculations predicted nearly complete co-migration of H atmospheres with dislocations, maintaining an approximately equilibrium atmosphere distribution. Given the even lower strain rate down to 10^{-7}/s in the present stress relaxation tests (Fig. 7), the pursuing of an equilibrated H-atmosphere is expected to be even more favorable. In these conditions where strain rate is so slow that extra force for atmosphere-drag [30,83,91] is not a significant matter, a factor predominating the dislocation glide resistance is interactions of segregated diffusible solutes with dislocation core [30,73,92]. That is, the core motion per atomic distance requires a simultaneous movement of those core solutes *via* their stress-assisted diffusion jump. Such a specific form of core interaction is usually designated as *diffusion-controlled glide* [30,73,92].

For H in dislocation cores in FCC metals and alloys, E_B of 0.1–0.16 eV has experimentally and analytically been reported [84–86,93,94]. The glide resistance due to core solute diffusion becomes important when $E_B > kT$— precisely the condition in the present study ($kT = 0.025$ eV at 295 K). Based on Friedel's model [92], the frequency of forward dislocation motion being accompanied by solute diffusion is given by:

$$\nu = \frac{1}{2}\nu_D \frac{b}{\lambda} \exp\left(- \frac{E_D - \tau^* b^2 \lambda}{kT} \right) \tag{14}$$

where ν_D is Debye frequency, λ is the average solute spacing along dislocation core, E_D is the activation energy for solute diffusion. Notably, a similar formulation was recently adopted by Matsumoto et al. to simulate H-dragged dislocation motion in α-Fe [95]. The $\tau^* b^2 \lambda$ term in eq. (14) reduces the diffusion energy barrier, making the forward jump of solutes in the direction of dislocation movement more feasible than their backward jump [30]. Potentially, it is this energy barrier, $E_D - \tau^* b^2 \lambda$, in Eq. (14) that is responsible for the H-induced extra glide resistance, ΔG_H, in Fig. 9 (c-2).

As the activation volume, V, is the stress derivative of activation energy (Eq. (3)), $\Delta G_H \approx E_D - \tau^* b^2 \lambda$ in Eq. (14) yields $V = b^2 \lambda$ for this *diffusion-controlled glide* process. Assuming λ spans a few Burgers vectors—a plausible estimate given the pronounced H segregation along dislocation cores (Section 5.3.3)—the resulting $b^2 \lambda$ contributes only a few b^3, orders of magnitude smaller than the experimentally measured V (Fig. 6). Moreover, another noticeable property of $b^2 \lambda$ is its stress-independence, seemingly consistent with the unchanged V–stress relationship in the presence of H, as seen in Fig. 6.

5.3.3. *H concentration- and stress-dependences of activation barrier*

The equilibrium partitioning of H into energetically favorable sites (*e.g.*, dislocations, grain boundaries, etc.) obeys Fermi-Dirac statistics [96]:

$$\frac{C_T}{1 - C_T} = \frac{C_0}{1 - C_0} \exp\left(\frac{E_B}{kT} \right) \tag{15}$$

where C_0 and C_T denote average and locally trapped H concentrations, respectively. Using $E_B \approx 0.13$ eV for dislocations in austenitic steels [84,86,93] and $T = 295$ K, Eq. (15) gives $C_T \approx 30$ at% and ≈ 60 at% for $C_0 = 2400$ and 8500 at ppm (*i.e.*, the concentrations in the present study), respectively. The calculation substantiates an extreme condensation of H along dislocation lines. From Eq. (15), we can also obtain a nearly proportional relationship between C_0 and C_T, when C_0 is in the range of 2000–10000 at ppm [10,23]. That is, the linear H concentration along dislocation core scales with the average H concentration. Suggestively, this proportionality between C_0 and C_T may underlie the previously identified $\propto C_0$ trend of H-induced solid solution-hardening [22,23]. Note that the simplicity of Eq. (15) may overestimate C_T since the number of possible solution sites for interstitial atoms should be limited even close to dislocation core. Nevertheless, such an overestimation does not affect the proportional trend between C_0 and C_T.

If the pre-exponential factor, $\dot{\gamma}_0$, remains unaffected by H, Eq. (1) allows estimation of ΔG_H when an increase in activation energy from ΔG_1 to ΔG_2 reduces the strain rate from $\dot{\gamma}_1$ to $\dot{\gamma}_2$:

$$\dot{\gamma}_1 / \dot{\gamma}_2 = \exp\left(\frac{\Delta G_2 - \Delta G_1}{kT} \right) \tag{16a}$$

$$\Delta G_H = \Delta G_2 - \Delta G_1 = kT \ln(\dot{\gamma}_1 / \dot{\gamma}_2) \tag{16b}$$

Here, the logarithmic term $\ln(\dot{\gamma}_1 / \dot{\gamma}_2)$ in eq. (16.b) corresponds to the offset along the $\ln(-\dot{\sigma})$ axis in Fig. 5. For example, taking the non-charged specimen as a reference state, the gap in $\ln(-\dot{\sigma})$ was 3.2 and 6.6 for 2400 and 8500 at ppm H, respectively, at a true strain of 0.02 (Section 4.4). These yield $\Delta G_H = 0.08$ and 0.17 eV. This $\Delta G_H = 0.17$ eV, being almost twice of 0.08 eV, does not scale with the ratio of C_0 between 8500 and 2400 at ppm. Instead, they can be ascribed to the C_T of 60 and 30 at%, suggesting the importance of H atoms along the dislocation core.

Fig. 10 (c) presents a refined schematic of H-influenced dislocation motion, incorporating diffusion-controlled *glide* into the *trough model* on a background of alloying elements. While the fundamental sketch remains as in Fig. 10 (b), the dislocation bulge must now carry an excess weight—H with the concentration of C_T and the activation barrier of $\Delta G_H \approx E_D - \tau^* b^2 \lambda$—during forward excursion. The necessity of external mechanical work for countervailing this ΔG_H leads to a higher effective stress and further smaller V, as depicted in Fig. 10 (c-1). Fig. 10 (c-1) reproduces the state already illustrated in Fig. 9 (c-3). As stress relaxes, V gradually approaches that of the non-charged specimen (Fig. 10 (c-2) and Fig. 9 (c-2)), while concomitant loss of the assistance by stress (*i.e.*, lesser compensation for ΔG_H) diminishes the likelihood of critical bulge nucleation, thereby slowing down the deformation. In an attempt to correlate these stress-dependent changes in V and strain rate in Fig. 10 (b)–(c) to Figs. 6 and 7, these figures are decorated with the same background color scheme.

Considering the still large V of $> 80b^3$ in H-charged specimens (Fig. 6), the bulge excursion process in Fig. 10 (c-1)–(c-2) may require a simultaneous diffusion jump of multiple H atoms inside the bulge. Assuming the average number of participating H atoms, N_H, is statistically determined to be nearly fixed value, the available bulge length, L_B, within a given time frame becomes narrower as the H-H spacing along dislocation core, L_H (λ in Eq. (14)), is reduced. Accordingly, $L_H \propto 1/N_H$ becomes proportional to L_B. Based on the considerations above, it is reasonable to assume that N_H is proportional to both C_0 and C_T, leading to "$L_B \propto 1/C_0$". Note that a reduction in L_H also diminishes the stress-assisted contribution in Eq. (14).

Approximating the bulge as a semi-circular arc with area $A = L_B^2 \theta / 6$ (*i.e.*, activation area in Fig. 10 (b) and (c)) [76], where θ is the excursion angle (Fig. 10 (b-1)), V is geometrically given by bA. Substituting this into eq. (11) and presuming sufficiently small θ [41], one reaches $S \propto 1/L_B$. Thus, we finally obtain $S \propto C_0$, rationalizing the previously identified proportionality between C_0 and resultant solid solution-hardening [22,23]. Such a relation holds when comparing the specimens with different H concentrations at a fixed strain rate where the available time for diffusion jump is constant. Whereas Fig. 10 (c-1)–(c-2) focuses on the high C_0 case, deformation at the same rate as Fig. 10 (b-1) is feasible at lower C_0 under stress levels in-between those in Fig. 10 (c-1) and (c-2). During stress relaxation from Fig. 10 (c-1) to (c-2), a greater number of H atoms would get a chance to migrate in some segments of the dislocation line with the aid of time. Consequently, even at constant L_H, the bulge size (*i.e.*, L_B, A, and V) gradually increases, reducing its formation stress in terms of the *trough model.* At larger L_H, the required stress further decreases due to the corresponding increase in L_B (Fig. 10 (c-3)). Specifically, Fig. 10 (c-3) illustrates the relaxation in the sample with 2400 at ppm H, where its stress falls below the flow stress in the non-charged condition.

In summary, H atoms along the dislocation core may limit the bulge length *via* their probability for stress-assisted forward diffusion. The dislocation bulge forms by overcoming energy troughs created by inherent alloying elements other than H. As H concentration increases, the available bulge length progressively decreases. Higher stress is then required for the nucleation of such shorter bulge. This required higher stress is an origin of H-induced solid solution-hardening.

5.4. *Summary and remaining tasks*

Our modeling of dynamic H–dislocation interaction establishes a new framework for interpreting H-induced modifications in the thermally activated flow of Fe-Cr-Ni austenitic steels. While some aspects remain qualitative, the combined mechanism of the *trough model* [76] and *diffusion-controlled glide* [30,73,92] effectively accounted for the following key phenomena:

I. Linear concentration-dependence of H-induced solid solution-hardening
II. A unified V-stress relationship across non- and H-charged specimens
III. Retardation of thermally activated flow by H under fixed stress and V

Identifying the rationales behind these macroscale features has significantly sharpened and advanced the understanding presented in our related previous publications [10–12,23].

However, the true character of the energy barrier underlying the *diffusion-controlled glide* of dislocation core (*i.e.*, the origin of E_{D} in eq. (14)) has not been uncovered yet. The activation energy for lattice H diffusion in austenite is typically 0.5–0.6 eV [24–26]. Although these diffusivities may be applied outside the core upon considering the potential gradient due to distorted lattice [30,83,91], it is still questionable whether such a simple assumption, even approximately, holds in the singularity field inside the core. Indeed, our estimation in Section 5.3.3 yielded ΔG_{H} of merely 0.08∼0.17 eV. Internal friction [97] and first-principles studies [98,99] have revealed attractive interactions between H atoms and substitutional Cr in austenite, attributed to their strong electrochemical affinity. Temporary formation of Cr–H complexes near dislocation core may hinder H migration by requiring additional energy for their dissociation. In FCC alloys with low to medium stacking fault energies (*e.g.*, $\approx$ 40 mJ/m^2 in Type310S [100]), specific interactions between interstitials and partial dislocation cores must also be considered [85,101]. Based on the precise quantification of ΔG_{H} per H atom and its dependency on alloy composition in future works, accounting for these complex effects will sophisticate our ever-evolving model into a more comprehensive form.

6. Conclusions

The thermally activated deformation behavior of H-charged Type310S austenitic steel was studied *via* stress relaxation tests of $\sim$1000 s. Specimens were uniformly pre-charged in 10 and 100 MPa H_2 gas environment at 543 K and subsequently tested at 295 K. Analysis of the relaxation curves and the stress-dependence of activation volume, V, revealed key aspects of macroscopic plasticity driven by the interplay of dislocations with H and alloying elements.

1. Solute H of $\sim$8500 at ppm caused solid solution-hardening up to $\approx$ 50 MPa through an increased effective stress. Due to this elevated stress, the extent of stress relaxation at a fixed strain became greater with an increasing H concentration. During stress relaxation, the H-induced effective stress was relaxed with the aid of time..
2. In all situations, V consistently became larger in the range of $\approx 80\sim200b^3$ as the stress decreased via the relaxation progressed. Such a stress-dependence of V reflected the property of rate-controlling obstacles. Although H initially reduced V owing to the solid solution-hardening-assisted elevated stress at the onset of relaxation, a unified V-stress relationship emerged for all H concentrations at a given strain.
3. At a given stress, plastic strain rate during relaxation was reduced (down to three orders of magnitude) with increasing H concentration. This is clear evidence for the role of H in slowing down the dislocation motion somehow, while the unified V-stress law indicates the absence of H-effect on the corresponding V.
4. The consistent V-stress relationship across non- and H-charged states demonstrates that the primary barriers resisting dislocations are still the obstacles inherently involved in the material—primarily alloying elements and forest dislocations—even under a high H concentration. Rather, H atoms dynamically segregate into a mobile dislocation and put an extra energy barrier in overcoming these intrinsic obstacles.

CRediT authorship contribution statement

Yuhei Ogawa: Writing – original draft, Investigation, Funding acquisition, Formal analysis, Data curation, Conceptualization. **Akinobu Shibata:** Writing – review & editing, Validation, Supervision, Conceptualization.

Declaration of competing interest

The authors declare that they have no known competing financial interests or personal relationships that could have appeared to influence the work reported in this paper.

Acknowledgements

This work was supported by JSPS KAKENHI (Grant No. 24K17180). Y.O. gratefully acknowledges Prof. Osamu Takakuwa (Kyushu University) and Prof. Kaneaki Tsuzaki (NIMS) for valuable scientific discussions. Technical support from the staff at the Research Center for Hydrogen Industrial Use and Storage (HYDROGENIUS), Kyushu University, in hydrogen-charging is also appreciated.

Supplementary materials

Supplementary material associated with this article can be found, in the online version, at doi:10.1016/j.actamat.2026.121896.

References

[1] T. Matsumoto, J. Eastman, H.K. Birnbaum, Direct observations of enhanced dislocation mobility due to hydrogen, Scr. Metall. 15 (1981) 1033–1037. https://doi.org/10.1016/0036-9748(81)90249-0.
[2] T. Boniszewski, G.C. Smith, The influence of hydrogen on the plastic deformation ductility, and fracture of nickel in tension, Acta Metall. 11 (1963) 165–178, https://doi.org/10.1016/0001-6160(63)90209-8.
[3] J.S. Blakemore, The portevin-le chatelier effect in hydrogenated nickel alloys, Metall. Mater. Trans. 1 (1970) 151–156, https://doi.org/10.1007/BF02819255.
[4] P.J. Ferreira, I.M. Robertson, H.K. Birnbaum, Hydrogen effects on the interaction between dislocations, Acta Mater. 46 (1998) 1749–1757, https://doi.org/10.1016/S1359-6454(97)00349-2.
[5] D.P. Abraham, C.J. Altstetter, The effect of hydrogen on the yield and flow stress of an austenitic stainless steel, Metall. Mater. Trans. A 26 (1995) 2849–2858, https://doi.org/10.1007/BF02669643.
[6] D.P. Abraham, C.J. Altstetter, Hydrogen-enhanced localization of plasticity in an austenitic stainless steel, Metall. Mater. Trans. A 26 (1995) 2859–2871, https://doi.org/10.1007/BF02669644.
[7] G. Girardin, D. Delafosse, Measurement of the saturated dislocation pinning force in hydrogenated nickel and nickel base alloys, Scr. Mater. 51 (2004) 1177–1181, https://doi.org/10.1016/j.scriptamat.2004.07.012.
[8] J.P. Chateau, D. Delafosse, T. Magnin, Numerical simulations of hydrogen–dislocation interactions in fcc stainless steels.: part I: hydrogen–dislocation interactions in bulk crystals, Acta Mater. 50 (2002) 1507–1522, https://doi.org/10.1016/S1359-6454(02)00008-3.
[9] V.N. Shivanyuk, J. Foct, V.G. Gavriljuk, Hydrogen-enhanced microplasticity of austenitic steels studied by means of internal friction, Mater. Sci. Eng.: A 300 (2001) 284–290, https://doi.org/10.1016/S0921-5093(00)01442-8.
[10] Y. Ogawa, M. Tanaka, T. Fujita, A. Shibata, Thermally activated dislocation motion in hydrogen-alloyed Fe–Cr–Ni austenitic steel revisited via Haasen plot, Int J Hydrog. Energy 74 (2024) 170–182, https://doi.org/10.1016/j.ijhydene.2024.06.113.
[11] Y. Ogawa, T. Fujita, Solid solution-hardening by hydrogen in Fe–Cr–Ni-based austenitic steel studied by strain rate sensitivity measurement: Contributions of effective stress and solute drag, Mater. Sci. Eng.: A 911 (2024) 146941, https://doi.org/10.1016/j.msea.2024.146941.
[12] Y. Ogawa, A. Shibata, Plastic flow in Fe-Cr-Ni austenitic steel under the presence of solute H: A study via room temperature creep, Acta Mater. (2024) 120659, https://doi.org/10.1016/j.actamat.2024.120659.
[13] P. Marshall, Austenitic Stainless Steels: Microstructure and Mechanical Properties, Springer, 1984.
[14] H.M. Ledbetter, M.W. Austin, Dilation of an fcc Fe–Cr–Ni alloy by interstitial carbon and nitrogen, Mater. Sci. Technol. (U. K.) 3 (1987) 101–104, https://doi.org/10.1179/mst.1987.3.2.101.

[15] M.L.G. Byrnes, M. Grujicic, W.S. Owen, Nitrogen strengthening of a stable austenitic stainless steel, Acta Metall. 35 (1987) 1853–1862, https://doi.org/10.1016/0001-6160(87)90131-3.

[16] K. Oda, N. Kondo, K. Shibata, X-ray absorption fine structure analysis of interstitial (C, N)-substitutional (Cr) complexes in austenitic stainless steels, ISIJ Int. 30 (1990) 625–631, https://doi.org/10.2355/isijinternational.30.625.

[17] N. Ohkubo, K. Miyakusu, Y. Uematsu, H. Kimura, Effect of alloying elements on the mechanical properties of the stable austenitic stainless steel, ISIJ Int. 34 (1994) 764–772, https://doi.org/10.2355/isijinternational.34.764.

[18] V.G. Gavriljuk, H. Berns, High Nitrogen Steels Structure, Properties, Manufacture, Applications, Springer, 1999.

[19] E. Werner, Solid solution and grain size hardening of nitrogen-alloyed austenitic steels, Mater. Sci. Eng.: A 101 (1988) 93–98, https://doi.org/10.1016/0921-5093(88)90054-8.

[20] K. Shibata, M. Kogita, C.-S. Chen, T. Fujita, Effects of carbon and silicon on softening in low-cycle fatigue of austenitic stainless steels, Trans. Iron Steel Inst. Jpn. 28 (1988) 406–412, https://doi.org/10.2355/isijinternational1966.28.406.

[21] J.C. Slater, Atomic radii in crystals, J. Chem. Phys. 41 (1964) 3199–3204, https://doi.org/10.1063/1.1725697.

[22] H. Nishida, Y. Ogawa, K. Tsuzaki, Chemical composition dependence of the strength and ductility enhancement by solute hydrogen in Fe–Cr–Ni-based austenitic alloys, Mater. Sci. Eng.: A 836 (2022) 142681, https://doi.org/10.1016/j.msea.2022.142681.

[23] Y. Ogawa, O. Takakuwa, K. Tsuzaki, Solid-solution hardening by hydrogen in Fe–Cr–Ni-based austenitic steel: Temperature and strain rate effects, Mater. Sci. Eng.: A (2023) 145281, https://doi.org/10.1016/j.msea.2023.145281.

[24] Y. Mine, T. Kimoto, Hydrogen uptake in austenitic stainless steels by exposure to gaseous hydrogen and its effect on tensile deformation, Corros. Sci. 53 (2011) 2619–2629, https://doi.org/10.1016/j.corsci.2011.04.022.

[25] C. San Marchi, B. Somerday, S. Robinson, Permeability, solubility and diffusivity of hydrogen isotopes in stainless steels at high gas pressures, Int J Hydrog. Energy 32 (2007) 100–116, https://doi.org/10.1016/j.ijhydene.2006.05.008.

[26] T. Perng, C.J. Altstetter, Effects of deformation on hydrogen permeation in austenitic stainless steels, Acta Metall. 34 (1986) 1771–1781, https://doi.org/10.1016/0001-6160(86)90123-9.

[27] M. Koyama, M. Rohwerder, C.C. Tasan, A. Bashir, E. Akiyama, K. Takai, D. Raabe, K. Tsuzaki, Recent progress in microstructural hydrogen mapping in steels: Quantification, kinetic analysis, and multi-scale characterisation, Mater. Sci. Technol. 33 (2017) 1481–1496, https://doi.org/10.1080/02670836.2017.1299276.

[28] H. Yu, A. Díaz, X. Lu, B. Sun, Y. Ding, M. Koyama, J. He, X. Zhou, A. Oudriss, X. Feaugas, Z. Zhang, Hydrogen embrittlement as a conspicuous material challenge-comprehensive review and future directions, Chem. Rev. 124 (2024) 6271–6392, https://doi.org/10.1021/acs.chemrev.3c00624.

[29] Y.G. Kim, J.M. Han, J.S. Lee, Composition and temperature dependence of tensile properties of austenitic Fe-Mn-Al-C alloys, Mater. Sci. Eng.: A 114 (1989) 51–59, https://doi.org/10.1016/0921-5093(89)90844-7.

[30] D. Caillard, J.L. Martin, Thermally Activated Mechanisms in Crystal Plasticity, 1st ed., Pergamon, 2003.

[31] H. Conrad, The athermal component of the flow stress in crystalline solids, Mater. Sci. Eng. 6 (1970) 265–273, https://doi.org/10.1016/0025-5416(70)90054-6.

[32] D. Hull, D.J. Bacon, Introduction to Dislocations, 3rd ed., Butterworth-Heinemann, 2011. https://doi.org/10.1016/C2009-0-64358-0.

[33] R.A. Mulford, Analysis of strengthening mechanisms in alloys by means of thermal-activation theory, Acta Metall. 27 (1979) 1115–1124, https://doi.org/10.1016/0001-6160(79)90129-9.

[34] W.A. Curtin, New interpretation of the Haasen plot for solute-strengthened alloys, Scr. Mater. 63 (2010) 917–920, https://doi.org/10.1016/j.scriptamat.2010.07.003.

[35] M. Niewczas, M. Jobba, R.K. Mishra, Thermally activated flow of dislocations in Al–Mg binary alloys, Acta Mater. 83 (2015) 372–382, https://doi.org/10.1016/j.actamat.2014.09.056.

[36] G. Laplanche, J. Bonneville, C. Varvenne, W.A. Curtin, E.P. George, Thermal activation parameters of plastic flow reveal deformation mechanisms in the CrMnFeCoNi high-entropy alloy, Acta Mater. 143 (2018) 257–264, https://doi.org/10.1016/j.actamat.2017.10.014.

[37] B.J. Diak, S. Saimoto, The determination of solute clusters in dilute aluminum alloys using strain rate sensitivity, Mater. Sci. Eng.: A 234–236 (1997) 1019–1022, https://doi.org/10.1016/S0921-5093(97)00342-0.

[38] U.F. Kocks, Superposition of Alloy Hardening, Strain Hardening, and Dynamic Recovery, in: Strength of Metals and Alloys, Elsevier, 1979: pp. 1661–1680. https://doi.org/10.1016/B978-1-4832-8412-5.50250-2.

[39] Z. Wu, Y. Gao, H. Bei, Thermal activation mechanisms and Labusch-type strengthening analysis for a family of high-entropy and equiatomic solid-solution alloys, Acta Mater. 120 (2016) 108–119, https://doi.org/10.1016/j.actamat.2016.08.047.

[40] Z.S. Basinski, R.A. Foxall, R. Pascual, Stress equivalence of solution hardening, Scr. Metall. 6 (1972) 807–814, https://doi.org/10.1016/0036-9748(72)90052-X.

[41] U.F. Kocks, A.S. Argon, M.F. Ashby, Thermodynamics and Kinetics of Slip, Prog. Mater. Sci. 19 (1975) 1–291. https://linkinghub.elsevier.com/retrieve/pii/0079642575900055.

[42] A.G. Evans, R.D. Rawlings, The thermally activated deformation of crystalline materials, Phys. Status Solidi 34 (1969) 9–31, https://doi.org/10.1002/pssb.19690340102.

[43] R.A. Mulford, U.F. Kocks, New observations on the mechanisms of dynamic strain aging and of jerky flow, Acta Metall. 27 (1979) 1125–1134, https://doi.org/10.1016/0001-6160(79)90130-5.

[44] U.F. Kocks, R.E. Cook, R.A. Mulford, Strain aging and strain hardening in Ni-C alloys, Acta Metall. 33 (1985) 623–638, https://doi.org/10.1016/0001-6160(85)90026-4.

[45] L.H. de Almeida, I. Le May, P.R.O. Emygdio, Mechanistic modeling of dynamic strain aging in austenitic stainless steels, Mater. Charact. 41 (1998) 137–150, https://doi.org/10.1016/S1044-5803(98)00031-X.

[46] C.W. Tien, C.J. Altstetter, Hydrogen-enhanced plasticity of 310S stainless steel, Mater. Chem. Phys. 35 (1993) 58–63, https://doi.org/10.1016/0254-0584(93)90177-N.

[47] Y. Hong, C. Zhou, Y. Zheng, J. Zheng, L. Zhang, X. Chen, Hydrogen effect on nanoindentation creep of austenitic stainless steel: A comparative study between primary creep stage and steady-state creep stage, Int. J. Hydrog. Energy 44 (2019) 22576–22583, https://doi.org/10.1016/j.ijhydene.2019.01.023.

[48] P. Spätig, J. Bonneville, J.-L. Martin, A new method for activation volume measurements: application to Ni3(Al,Hf), Mater. Sci. Eng.: A 167 (1993) 73–79, https://doi.org/10.1016/0921-5093(93)90339-G.

[49] S. Saimoto, The Characterization of Materials by Precision Strain Rate Sensitivity, J. Eng. Mater. Technol. 109 (1987) 230–235, https://doi.org/10.1115/1.3225969.

[50] W. Bochniak, The cottrell-stokes law for F.C.C. single crystals, Acta. Metall. Mater. 41 (1993) 3133–3140, https://doi.org/10.1016/0956-7151(93)90043-R.

[51] K. Prasad, V. Balaji, H. Krishnaswamy, P.S. Phani, P. Carlone, Rigorous analysis and pragmatic guidelines in estimating strain rate sensitivity using stress relaxation test, Mech. Mater. 168 (2022) 104279, https://doi.org/10.1016/j.mechmat.2022.104279.

[52] A.S. Krausz, B. Faucher, On the stress dependence of the experimental activation volume, Scr. Metall. 14 (1980) 53–57, https://doi.org/10.1016/0036-9748(80)90123-4.

[53] K. Saitou, T. Hikage, Activation Volume in Tensile Deformation of Cu-Ni Single Crystals, J. Jpn. Inst. Met. 49 (1985) 344–351, https://doi.org/10.2320/jinstmet1952.49.5_344.

[54] K. Tanoue, Thermal activation analysis on the plastic deformation satisfied with the Cottrell-Stokes law, Acta Metall. Mater. 40 (1992) 1945–1950, https://doi.org/10.1016/0956-7151(92)90180-M.

[55] Y. Ogawa, H. Hosoi, K. Tsuzaki, T. Redarce, O. Takakuwa, H. Matsunaga, Hydrogen, as an alloying element, enables a greater strength-ductility balance in an Fe-Cr-Ni-based, stable austenitic stainless steel, Acta Mater. 199 (2020) 181–192, https://doi.org/10.1016/j.actamat.2020.08.024.

[56] F. Guiu, P.L. Pratt, Stress Relaxation and the Plastic Deformation of Solids, Phys. Status Solidi 6 (1964) 111–120, https://doi.org/10.1002/pssb.19640060108.

[57] S.P. Hannula, M.A. Korhonen, C.Y. Li, Strain aging and load relaxation behavior of type 316 stainless steel at room temperature, Metall. Trans. A 17 (1986) 1757–1767, https://doi.org/10.1007/BF02817274.

[58] K.S.B. Rose, S.G. Gloverj, A study of strain-ageing in austenite, Acta Metall. 14 (1966) 1505–1516, https://doi.org/10.1016/0001-6160(66)90172-6.

[59] J.L. Martin, T. Kruml, Characterizing thermally activated dislocation mobility, J. Alloys. Compd. 378 (2004) 2–12, https://doi.org/10.1016/j.jallcom.2003.10.063.

[60] J.L. Martin, B. Lo Piccolo, T. Kruml, J. Bonneville, Characterization of thermally activated dislocation mechanisms using transient tests, Mater. Sci. Eng.: A 322 (2002) 118–125, https://doi.org/10.1016/S0921-5093(01)01124-8.

[61] X.-S. Yang, Y.-J. Wang, G.-Y. Wang, H.-R. Zhai, L.H. Dai, T.-Y. Zhang, Time, stress, and temperature-dependent deformation in nanostructured copper: Stress relaxation tests and simulations, Acta Mater. 108 (2016) 252–263, https://doi.org/10.1016/j.actamat.2016.02.021.

[62] V. Balaji, S. Kumar, H. Krishnaswamy, R.K. Digavalli, M.G. Lee, F. Barlat, Transient stress relaxation test to identify material constants in dislocation density model, Metall. Mater. Trans. A 53 (2022) 1969–1990, https://doi.org/10.1007/s11661-022-06624-2.

[63] H. Neuhäuser, H. Flor, Variation of obstacle strength during stress relaxation of α-brass single crystals, Scr. Metall. 12 (1978) 443–448, https://doi.org/10.1016/0036-9748(78)90254-5.

[64] H. Flor, H.J. Gudladt, C. Schwink, Plastic deformation of Fe-Ni invar alloys, Acta Metall. 28 (1980) 1611–1619, https://doi.org/10.1016/0001-6160(80)90014-0.

[65] T. Ito, Y. Ogawa, W. Gong, W. Mao, T. Kawasaki, K. Okada, A. Shibata, S. Harjo, Role of solute hydrogen on mechanical property enhancement in Fe–24Cr–19Ni austenitic steel: An in situ neutron diffraction study, Acta Mater. 287 (2025) 120767, https://doi.org/10.1016/j.actamat.2025.120767.

[66] E. Sirois, H.K. Birnbaum, Effects of hydrogen and carbon on thermally activated deformation in nickel, Acta Metall. Mater. 40 (1992) 1377–1385, https://doi.org/10.1016/0956-7151(92)90438-K.

[67] D.M. Oliveira, C.W. San Marchi, D.L. Medlin, J.C. Gibeling, Hydrogen influences thermal activation parameters for dislocation glide during low cycle fatigue of 316L stainless steel, Mater. Sci. Eng.: A 932 (2025) 148243, https://doi.org/10.1016/j.msea.2025.148243.

[68] Y. Estrin, H. Mecking, A unified phenomenological description of work hardening and creep based on one-parameter models, Acta Metall. 32 (1984) 57–70, https://doi.org/10.1016/0001-6160(84)90202-5.

[69] H. Mecking, U.F. Kocks, Kinetics of flow and strain-hardening, Acta Metall. 29 (1981) 1865–1875, https://doi.org/10.1016/0001-6160(81)90112-7.

[70] T.H. Alden, Theory of mobile dislocation density: Application to the deformation of 304 stainless steel, Metall. Trans. A 18 (1987) 51–62, https://doi.org/10.1007/BF02646221.

[71] L. Lu, T. Zhu, Y. Shen, M. Dao, K. Lu, S. Suresh, Stress relaxation and the structure size-dependence of plastic deformation in nanotwinned copper, Acta Mater. 57 (2009) 5165–5173, https://doi.org/10.1016/j.actamat.2009.07.018.
[72] G.M. Castelluccio, C.B. Geller, D.L. McDowell, A rationale for modeling hydrogen effects on plastic deformation across scales in FCC metals, Int. J. Plast. 111 (2018) 72–84, https://doi.org/10.1016/j.ijplas.2018.07.009.
[73] P.M. Anderson, J.P. Hirth, J. Lothe, Theory of Dislocations, 3rd ed., Cambridge University Press, 2017.
[74] M.Z. Butt, P. Feltham, Solid-solution hardening, J. Mater. Sci. 28 (1993) 2557–2576, https://doi.org/10.1007/BF00356192.
[75] P. Feltham, Solid solution hardening of metal crystals, J. Phys. D. Appl. Phys. 1 (1968) 305, https://doi.org/10.1088/0022-3727/1/3/305.
[76] U.F. Kocks, Kinetics of solution hardening, Metall. Trans. A 16 (1985) 2109–2129, https://doi.org/10.1007/BF02670415.
[77] J.C. Fisher, Application of Cottrell's theory of yielding to delayed yield in steel, Trans. ASM 47 (1955) 451–462.
[78] N. Tsuchida, Application of the Kocks–Mecking model to tensile deformation of an austenitic 25Cr–19Ni steel, Acta Mater. 49 (2001) 3029–3038, https://doi.org/10.1016/S1359-6454(01)00197-5.
[79] P.S. Follansbee, U.F. Kocks, A constitutive description of the deformation of copper based on the use of the mechanical threshold stress as an internal state variable, Acta Metall. 36 (1988) 81–93, https://doi.org/10.1016/0001-6160(88)90030-2.
[80] J. Tien, A.W. Thompson, I.M. Bernstein, R.J. Richards, Hydrogen transport by dislocations, Metall. Trans. A 7 (1976) 821–829, https://doi.org/10.1007/BF02644079.
[81] T. Zirkle, L. Costello, D.L. McDowell, Crystal plasticity modeling of hydrogen and hydrogen-related defects in initial yield and plastic flow of single-crystal stainless Steel 316L, Metall. Mater. Trans. A 52 (2021) 3961–3977, https://doi.org/10.1007/s11661-021-06357-8.
[82] E.N. Epperly, R.B. Sills, Transient solute drag and strain aging of dislocations, Acta Mater. 193 (2020) 182–190, https://doi.org/10.1016/j.actamat.2020.03.031.
[83] R.B. Sills, W. Cai, Solute drag on perfect and extended dislocations, Philos. Mag. 96 (2016) 895–921, https://doi.org/10.1080/14786435.2016.1142677.
[84] X.W. Zhou, C. Nowak, R.S. Skelton, M.E. Foster, J.A. Ronevich, C. San Marchi, R. B. Sills, An Fe–Ni–Cr–H interatomic potential and predictions of hydrogen-affected stacking fault energies in austenitic stainless steels, Int J Hydrog. Energy 47 (2022) 651–665, https://doi.org/10.1016/j.ijhydene.2021.09.261.
[85] Y. Tang, J.A. El-Awady, Atomistic simulations of the interactions of hydrogen with dislocations in fcc metals, Phys. Rev. B Condens. Matter. Mater. Phys. 86 (2012) 1–13, https://doi.org/10.1103/PhysRevB.86.174102.
[86] A. Atrens, N.F. Fiore, K. Miura, Dislocation damping and hydrogen pinning in austenitic stainless steels, J. Appl. Phys. 48 (1977) 4247–4251, https://doi.org/10.1063/1.323410.
[87] R. Kirchheim, Reducing grain boundary, dislocation line and vacancy formation energies by solute segregation. I. Theoretical background, Acta Mater. 55 (2007) 5129–5138, https://doi.org/10.1016/j.actamat.2007.05.047.
[88] R. Kirchheim, Revisiting hydrogen embrittlement models and hydrogen-induced homogeneous nucleation of dislocations, Scr. Mater. 62 (2010) 67–70, https://doi.org/10.1016/j.scriptamat.2009.09.037.
[89] D.G. Ulmer, C.J. Altstetter, Phase relations in the hydrogen-austenite system, Acta Metall. Mater. 41 (1993) 2235–2241, https://doi.org/10.1016/0956-7151(93)90393-7.
[90] Y. Estrin, L.P. Kubin, Local strain hardening and nonuniformity of plastic deformation, Acta Metall. 34 (1986) 2455–2464, https://doi.org/10.1016/0001-6160(86)90148-3.
[91] H. Yoshinaga, S. Morozumi, The solute atmosphere round a moving dislocation and its dragging stress, Philos. Mag.: J. Theor. Exp. Appl. Phys. 23 (1971) 1367–1385, https://doi.org/10.1080/14786437108217008.
[92] J. Friedel, Dislocations, 1st ed, Pergamon Press, 1964.
[93] Y. Yagodzinskyy, M. Ivanchenko, H. Hänninen, Hydrogen-dislocation interaction in austenitic stainless steel studied with mechanical loss spectroscopy, Solid State Phenom. 184 (2012) 227–232, https://doi.org/10.4028/www.scientific.net/SSP.184.227.
[94] M. Yamaguchi, M. Itakura, T. Tsuru, K. Ebihara, Hydrogen-trapping energy in screw and edge dislocations in aluminum: first-principles calculations, Mater Trans 62 (2021) 582–589, https://doi.org/10.2320/matertrans.MT-M2020375.
[95] R. Matsumoto, S.T. Oyinbo, M. Vijendran, S. Taketomi, Hydrogen effect on the mobility of edge dislocation in α-iron: a long-timescale molecular dynamics simulation, ISIJ Int. 62 (2022), https://doi.org/10.2355/isijinternational.ISIJINT-2022-311. ISIJINT-2022-311.
[96] J.P. Hirth, Effects of hydrogen on the properties of iron and steel, Metall. Trans. A 11 (1980) 861–890, https://doi.org/10.1007/BF02654700.
[97] V.G. Gavriljuk, H. Haänninen, S.Y.U. Smouk, A.V. Tarasenko, K. Ullakko, Internal friction in hydrogen-charged CrNi and CrNiMn austenitic stainless steels, Met. Mater Trans Phys Met. Mater Sci 27 (1996) 1815–1821, https://doi.org/10.1007/BF02651931.
[98] J. Moriyama, O. Takakuwa, M. Yamaguchi, Y. Ogawa, K. Tsuzaki, The contribution of Cr and Ni to hydrogen absorption energy in Fe-Cr-Ni austenitic systems: A first-principles study, Comput. Mater. Sci. 232 (2024) 112650, https://doi.org/10.1016/j.commatsci.2023.112650.
[99] J. Moriyama, M. Yamaguchi, O. Takakuwa, Effects of antagonistic interaction between Cr and Ni on hydrogen solubility in a Fe-Cr-Ni ternary austenitic system: A first-principles calculation, Mater. Today Commun. 40 (2024) 110059, https://doi.org/10.1016/j.mtcomm.2024.110059.
[100] C.G. Rhodes, A.W. Thompson, The composition dependence of stacking fault energy in austenitic stainless steels, Metall. Trans. A 8 (1977) 1901–1906, https://doi.org/10.1007/BF02646563.
[101] R. Xie, S. Lu, W. Li, Y. Tian, L. Vitos, Dissociated dislocation-mediated carbon transport and diffusion in austenitic iron, Acta Mater. 191 (2020) 43–50, https://doi.org/10.1016/j.actamat.2020.03.042.